aerospace

MDPI

Article

A Space Non-Cooperative Target Rendezvous Orbit Prediction and Control Method Based on Active Disturbance Rejection

Lin Dai [1,2,*], Hongyuan Wang [2], Zaiming Jiang [1], Zhiqiang Yan [2] and Yang Zhang [3,*]

[1] Overall Design Department, Beijing Institute of Mechanical and Electrical Engineering, Beijing 100854, China
[2] Research Center for Space Optical Engineering, Harbin Institute of Technology, Harbin 150001, China
[3] Aerospace Information Research Institute, Chinese Academy of Sciences, Beijing 100094, China
* Correspondence: dailin_0000@163.com (L.D.); zhangyang101002@aircas.ac.cn (Y.Z.)

Abstract

Aiming at the problems of strong model uncertainty, unmodeled perturbation disturbances and unknown maneuvering of space non-cooperative targets in orbital rendezvous missions, an orbit prediction and control method combining active disturbance rejection and model predictive control (ADRC-MPC) is proposed in this paper. Firstly, the relative motion dynamic equations of chaser–target are established under a geocentric inertial coordinate system, and the lumped disturbance including space perturbation and unknown evasive maneuvers of the target is expanded into extended state variable. Secondly, an extended state observer (ESO) is designed to achieve real-time accurate estimation and feedforward compensation of time-varying lumped disturbances, which mitigates adverse influences induced by J2 zonal harmonics, atmospheric drag, solar radiation pressure, and target evasive maneuvers. Thirdly, a constrained MPC strategy incorporating thrust saturation, approach corridor, and collision safety zone constraints is developed. Sufficient conditions for closed-loop input-to-state stability (ISS) are theoretically derived via the small-gain theorem under the given assumptions, which ensures the uniform ultimate boundedness (UUB) of tracking errors. Finally, numerical simulations, comparative benchmarks against conventional MPC and proportional-derivative (PD) control, and Monte Carlo robustness tests are performed. Simulation results demonstrate that the proposed ADRC-MPC framework delivers superior rendezvous precision, stronger disturbance rejection, reduced propellant consumption, and improved robustness against initial state offsets and measurement noises, laying solid theoretical and technical foundations for autonomous orbital rendezvous with space non-cooperative targets.

Keywords: non-cooperative target; orbital rendezvous; active disturbance rejection; predictive control; extended state observer; relative motion

Check for updates

Academic Editor: Vladimir S. Aslanov

Received: 18 July 2026
Revised: 18 August 2026
Accepted: 21 August 2026
Published: 28 August 2026

Copyright: © 2026 by the authors. Licensee MDPI, Basel, Switzerland. This article is an open access article distributed under the terms and conditions of the Creative Commons Attribution (CC BY) license.

1. Introduction

In this paper, the target satellite is considered a non-cooperative target. It is defined as a space object that lacks communication capabilities, dedicated navigation aids, and the ability or willingness to perform coordinated maneuvers with the chaser. Consequently, all relative state measurements, trajectory predictions, and control decisions must be performed autonomously by the chaser. The chaser has no prior knowledge of the target's orbital parameters, aerodynamic characteristics, or potential maneuvers, making robust disturbance rejection a critical requirement for successful rendezvous.

With the rapid development of on-orbit servicing, active debris removal, and close-proximity operations, high-precision orbit prediction and robust control for non-cooperative

space targets have become critical and challenging research topics in astrodynamics [1,2]. Non-cooperative targets typically lack communication links, orbital state broadcasting, and attitude information, and their motion is inevitably affected by complex space perturbations, including J2 gravitational perturbations, atmospheric drag, third-body gravitational effects, and solar radiation pressure [3,4]. In addition, unknown target maneuvers may further introduce unmodeled disturbances [5,6]. These factors lead to strong uncertainties, high nonlinearity, and limited measurement information in relative motion dynamics, which seriously restrict the safety, accuracy, and reliability of rendezvous and proximity operations [7].

In recent years, considerable efforts have been devoted to relative motion control for spacecraft rendezvous. Model predictive control (MPC) has been widely utilized due to its remarkable ability to handle multivariable constraints and optimize future trajectories explicitly. Hartley developed a constrained MPC scheme for spacecraft rendezvous with thrust and approach-corridor constraints [8,9]. Weiss proposed a series of MPC strategies with explicit constraint handling and case studies for rendezvous and docking [10]. Against the background of spacecraft rendezvous and docking with non-cooperative targets, Iskender conducted research on guidance and control methods based on model predictive control [11]. However, traditional MPC relies heavily on the accuracy of the nominal dynamical model [12]. When facing unmodeled dynamics, unknown target maneuvers, and strong environmental disturbances, its robustness and estimation ability are limited [13].

To alleviate model sensitivity, tube-based robust MPC (TRMPC) dominates recent robust MPC studies. TRMPC constructs disturbance invariant tubes to separate nominal trajectory planning and uncertainty feedback correction, avoiding the heavy computation of min–max robust MPC. Recent works designed adaptive tube tightening rules for circular/elliptical orbit proximity missions [14–16]. However, existing TRMPC uses fixed disturbance bounds, leading to excessive conservatism under time-varying target maneuvers; few integrate online lumped disturbance estimation to distinguish environmental perturbations and active target maneuvers. Chance-constrained and Lyapunov robust MPC further requires prior disturbance distribution or sacrifice multi-constraint handling capacity, limiting onboard real-time application.

Active disturbance rejection control (ADRC) and extended state observers (ESO) have been introduced to estimate and compensate for lumped disturbances in real time without requiring an accurate disturbance model [17,18]. Nevertheless, conventional ADRC is essentially a feedback compensation strategy and lacks the capability of trajectory prediction and multi-constraint optimization, which is essential for safe rendezvous [19].

Learning-based MPC emerged as a data-driven branch from 2023 to 2026 to reduce model dependence. Imitation learning MPC trains neural policies from safe NMPC trajectories to cut online computation cost, while reinforcement learning MPC improves adaptability to random initial errors. Unfortunately, nearly all learning MPC schemes lack rigorous closed-loop stability proof and demand massive offline training datasets; their tracking performance degrades sharply under unseen large-amplitude target evasive maneuvers, ignoring long-term orbital perturbation coupling.

Sliding mode control (SMC) is another mainstream robust control for uncertain rendezvous systems. Recent fractional-order adaptive SMC and neural SMC achieve finite-time error convergence with input saturation suppression [20]. Hybrid SMC–MPC cascaded structures combine SMC robustness and MPC constraint processing capacity, but most designs only stack two control loops without unified small-gain/ISS stability analysis. Moreover, SMC disturbance observers exhibit a slower response for fast time-varying target maneuvers compared with ESO, bringing larger transient overshoot; pure SMC cannot pre-plan constrained trajectories within safety approach corridors.

Some efforts have been made to combine ESO and MPC for disturbed systems. However, most existing applications adopt a straightforward cascade framework without theoretical stability guarantees [21,22]. Furthermore, few studies simultaneously consider high-order orbital perturbations, unknown target maneuvers, closed-loop stability, and constrained optimization in a unified framework for non-cooperative target rendezvous. In particular, the lack of theoretical guarantees for closed-loop stability and robustness remains a critical limitation for engineering validation [23,24].

In summary, although relevant research on relative motion modeling, active disturbance rejection estimation, and model predictive control for space non-cooperative target rendezvous has achieved certain progress, there still exist several key scientific and technical problems to be solved urgently. Most existing orbital control methods rely heavily on the accuracy of nominal dynamic models and cannot effectively cope with compound uncertain disturbances composed of high-order orbital perturbations, such as J2 gravitational perturbation, atmospheric drag, solar radiation pressure, as well as unknown time-varying maneuvering of non-cooperative targets. It is difficult to simultaneously suppress environmental perturbation and target maneuver disturbance under a unified framework. The existing combined control strategies of extended state observer and model predictive control mostly adopt a simple cascade structure, lacking rigorous closed-loop stability theoretical demonstration. Most methods only rely on numerical simulation to verify the effect, without strict theoretical proof of input-to-state stability and uniform ultimate boundedness of tracking error, which restricts their practical engineering application. Traditional rendezvous control research seldom comprehensively considers multiple physical constraints including thrust saturation, approach corridor and safety collision avoidance zone in the controller design process. Moreover, there is a lack of systematic quantitative comparison with classic control methods such as PD and pure MPC, as well as sufficient robustness verification under initial state deviation, thruster parameter error and seeker measurement noise. In addition, few studies take into account the real-time computing performance of the algorithm on space-borne platforms and the optimal balance among rendezvous accuracy, convergence time and propellant consumption, which makes it difficult to directly support autonomous on-orbit rendezvous tasks of non-cooperative targets.

Motivated by the above challenges, this paper proposes a novel orbit prediction and control method for non-cooperative target rendezvous based on active disturbance rejection and constrained model predictive control. The lumped disturbance, including environmental perturbations and unknown target maneuvers, is estimated online by an extended state observer [25]. A constrained MPC is designed to achieve high-precision trajectory tracking while satisfying physical constraints [26,27]. More importantly, the closed-loop input-to-state stability (ISS) is rigorously proven to ensure robustness and convergence [28,29].

The main contributions and novelties of this paper are summarized as follows:

(1) A novel integrated ADRC-MPC control framework is proposed for non-cooperative target rendezvous, which unifies real-time lumped disturbance estimation, high-precision trajectory tracking, and multi-constraint optimization within a systematic design. This framework can simultaneously suppress J2, atmospheric drag, third-body perturbation, solar radiation pressure, and unknown target maneuvers [30].

(2) Rigorous closed-loop input-to-state stability (ISS) analysis under explicit sufficient conditions is presented using the small-gain theorem. Under the proposed modeling and control assumptions, we theoretically demonstrate that the tracking error is uniformly ultimately bounded (UUB) under unknown time-varying disturbances, which provides a theoretical foundation for engineering applications.

(3) A constraint-aware predictive control scheme with practical physical constraints (thrust magnitude, approach corridor, safety zone) is developed. Compared with conventional MPC and ADRC, the proposed method achieves stronger robustness, higher tracking accuracy, and lower fuel consumption under severe disturbances.

To clearly differentiate the contributions of this study from state-of-the-art techniques, Table 1 provides a comparison across four key research dimensions.

Table 1. Comparison of advantages and disadvantages of different methods.

Research Dimension	Existing ADRC-MPC/Robust MPC/Adaptive Control Literature	The Proposed ADRC-MPC Scheme in This Work
Disturbance Modeling and ESO Architecture	Separate observers for orbital perturbations and target maneuvers; ESO only provides static feedforward compensation without prediction capacity; fixed ESO bandwidth incapable of adapting to diverse time-varying disturbances	Unified lumped disturbance augmented into system states and embedded in MPC receding prediction; ESO bandwidth adaptively adjusted via pole placement to realize receding predictive disturbance compensation
Simulation Disturbance Configuration	Only single step/sinusoidal target maneuver applied, decoupled from orbital environmental perturbations	Coupled four environmental perturbations (J2, atmospheric drag, lunar–solar gravity, solar radiation pressure) plus three types of target evasive maneuvers (sinusoidal/step/ramp), joint multi-source disturbance simulations
Completeness of Robustness Verification	Insufficient coverage of uncertainty items in random simulations	100 Monte Carlo cases covering triaxial initial position/velocity deviations, thruster parameter drifts, full-range systematic and stochastic radar ranging/velocity measurement noise in X/Y/Z axes
Controller Optimization Objective	Single objective: minimize position tracking error only, unable to balance convergence time and propellant usage	Weighted cost function integrating position error, velocity error and control thrust to achieve comprehensive optimality of tracking accuracy, convergence speed and fuel consumption

2. Relative Motion Equations for Spatial Orbital Rendezvous

The motion equations of the chaser satellite and target satellite in the geocentric first equatorial coordinate system are as follows [31]:

$$\begin{cases} \dot{V}x_M = -\dfrac{\mu x_M}{r_M^3} + \sum\limits_{i=1}^{5} A_{Mxi} + u_{Mx} \\ \dot{V}y_M = -\dfrac{\mu y_M}{r_M^3} + \sum\limits_{i=1}^{5} A_{Myi} + u_{My} \\ \dot{V}z_M = -\dfrac{\mu z_M}{r_M^3} + \sum\limits_{i=1}^{5} A_{Mzi} + u_{Mz} \\ \dot{x}_M = Vx_M \\ \dot{y}_M = Vy_M \\ \dot{z}_M = Vz_M \\ r_M = \sqrt{x_M^2 + y_M^2 + z_M^2} \end{cases} \tag{1}$$

$$\begin{cases} \dot{V}x_T = -\dfrac{\mu x_T}{r_T^3} + \sum\limits_{i=1}^{5} A_{Txi} + u_{Tx} \\ \dot{V}y_T = -\dfrac{\mu y_T}{r_T^3} + \sum\limits_{i=1}^{5} A_{Tyi} + u_{Ty} \\ \dot{V}z_T = -\dfrac{\mu z_T}{r_T^3} + \sum\limits_{i=1}^{5} A_{Tzi} + u_{Tz} \\ \dot{x}_T = Vx_T \\ \dot{y}_T = Vy_T \\ \dot{z}_T = Vz_T \\ r_T = \sqrt{x_T^2 + y_T^2 + z_T^2} \end{cases} \tag{2}$$

The geocentric first equatorial coordinate system is adopted in this paper, and its detailed definition is provided as follows: The origin O of the coordinate system is located at the Earth's center of mass. The OX-axis lies within the equatorial plane and points toward the vernal equinox; the OZ-axis is perpendicular to the equatorial plane and aligns with the angular velocity vector of Earth's rotation. The OY-axis is orthogonal to both the OX-axis and the OZ-axis, and the frame OXYZ forms a right-handed Cartesian coordinate system.

In the above equations, x_M, y_M, z_M, Vx_M, Vy_M, and Vz_M represent the position and velocity of the chaser satellite in the three directions of the geocentric first equatorial coordinate system, respectively; x_T, y_T, z_T, Vx_T, Vy_T, and Vz_T represent the position and velocity of the target satellite in the three directions of the geocentric first equatorial coordinate system, respectively. μ denotes the gravitational constant of the Earth, with a value of $3.986004418 \times 10^{14}$ m^3/s^2.

$A_{M(T)x/y/z1}$, $A_{M(T)x/y/z2}$, $A_{M(T)x/y/z3}$, $A_{M(T)xy/z4}$, $A_{M(T)x/y/z5}$, and $u_{M(T)x/y/z}$ respectively represent the non-spherical gravitational perturbation acceleration, atmospheric drag-induced acceleration, solar gravitational acceleration, lunar gravitational acceleration, solar radiation pressure-induced acceleration, and self-applied control acceleration acting on the chaser satellite (target satellite) in the X (Y/Z)-direction of the geocentric first equatorial coordinate system. Among them are $u_{Mx} \in \mathbb{R}$, $u_{My} \in \mathbb{R}$, $u_{Mz} \in \mathbb{R}$; $u_{Tx} \in \mathbb{R}$, $u_{Ty} \in \mathbb{R}$, and $u_{Tz} \in \mathbb{R}$.

Taking the X-direction of the chaser satellite as an example, the calculation expressions for the aforementioned perturbation accelerations are as follows:

$$A_{Mx1} = \frac{\mu x_M a_e^2}{r_M^5} J_2 [-1.5 + 7.5(\frac{z_M}{r_M})^2] \tag{3}$$

$$A_{Mx2} = -\frac{1}{2} \frac{C_{DM} \rho S_M}{m_M} V'_M (Vx_M + y_M \omega_e) \tag{4}$$

$$A_{Mx3} = M_s \mu (\frac{x_s - x_M}{\Delta r_M^3} - \frac{x_s}{r_s^3}) \tag{5}$$

$$A_{Mx4} = M_r \mu (\frac{x_r - x_M}{\Delta r_M'^3} - \frac{x_r}{r_r^3}) \tag{6}$$

$$A_{Mx5} = \frac{K \rho_M S_M}{m_M} \frac{x_M - x_s}{\Delta r_M} \tag{7}$$

a_e is the Earth's equatorial radius, with a value of 6,378,140 m; J_2 is the Earth's gravitational field harmonic coefficient, with a value of $1.082629832258 \times 10^{-3}$; C_{DM} is the drag coefficient; ρ is the atmospheric density; S_M is the characteristic area; m_M is the mass of the chaser satellite; ω_e is the Earth's angular velocity, with a value of $7292115.0 \times 10^{-11}$ rad/s. M_s is the Sun–Earth mass ratio, with a value of 332,946.0; Δr_M is the distance between the Sun and the chaser satellite; M_r is the Moon–Earth mass ratio, with a value of 0.01230002; $\Delta r'_M$ is the distance between the Moon and the chaser satellite; K is the solar radiation

pressure constant, with a value of 4.5×10^{-6} N/m^2; ρ_M is the surface reflection characteristic coefficient of the satellite, with a value of 1 for full absorption, 1.44 for perfect diffuse reflection, and 2 for perfect specular reflection; S_M is the projected area of the satellite perpendicular to the direction of sunlight.

Based on Equations (1) and (2), the relative motion equation of the chaser satellite and the target satellite is obtained as follows:

$$\begin{cases} \Delta\dot{V}x = \dot{V}x_M - \dot{V}x_T = -\mu(\frac{x_M}{r_M^3} - \frac{x_T}{r_T^3}) + \sum_{i=1}^{5} A_{Mxi} - \sum_{i=1}^{5} A_{Txi} + (u_{Mx} - u_{Tx}) \\ \Delta\dot{V}y = \dot{V}y_M - \dot{V}y_T = -\mu(\frac{y_M}{r_M^3} - \frac{y_T}{r_T^3}) + \sum_{i=1}^{5} A_{Myi} - \sum_{i=1}^{5} A_{Tyi} + (u_{My} - u_{Ty}) \\ \Delta\dot{V}z = \dot{V}z_M - \dot{V}z_T = -\mu(\frac{z_M}{r_M^3} - \frac{z_T}{r_T^3}) + \sum_{i=1}^{5} A_{Mzi} - \sum_{i=1}^{5} A_{Tzi} + (u_{Mz} - u_{Tz}) \\ \Delta\dot{x} = \dot{x}_M - \dot{x}_T = Vx_M - Vx_T \\ \Delta\dot{y} = \dot{y}_M - \dot{y}_T = Vy_M - Vy_T \\ \Delta\dot{z} = \dot{z}_M - \dot{z}_T = Vz_M - Vz_T \end{cases} \tag{8}$$

The inputs for the rendezvous orbit control design include the accelerations of the chaser satellite in the three directions of the first equatorial coordinate system. The terminal condition requires that the position and velocity of the chaser satellite coincide with those of the target satellite at time t_f, i.e., Δx, Δy, Δz, ΔVx, ΔVy, and ΔVz are all zero.

3. Active Disturbance Rejection-Based Predictive Control Method for Rendezvous Orbits

To address the aforementioned orbital rendezvous control problem, the rendezvous control problem is addressed by the proposed ADRC-MPC framework, which is designed to handle both known orbital perturbations and unknown target maneuvers. Meanwhile, model predictive control (MPC) is adopted to calculate and generate control commands, which adjust the dynamic responses of relative position and relative velocity during rendezvous with the target in real time, so as to meet the requirements of rendezvous time, rendezvous control precision, and propellant consumption for orbital control during the rendezvous process. The design flow chart of the active disturbance rejection-based predictive control system for rendezvous orbits is shown in Figure 1.

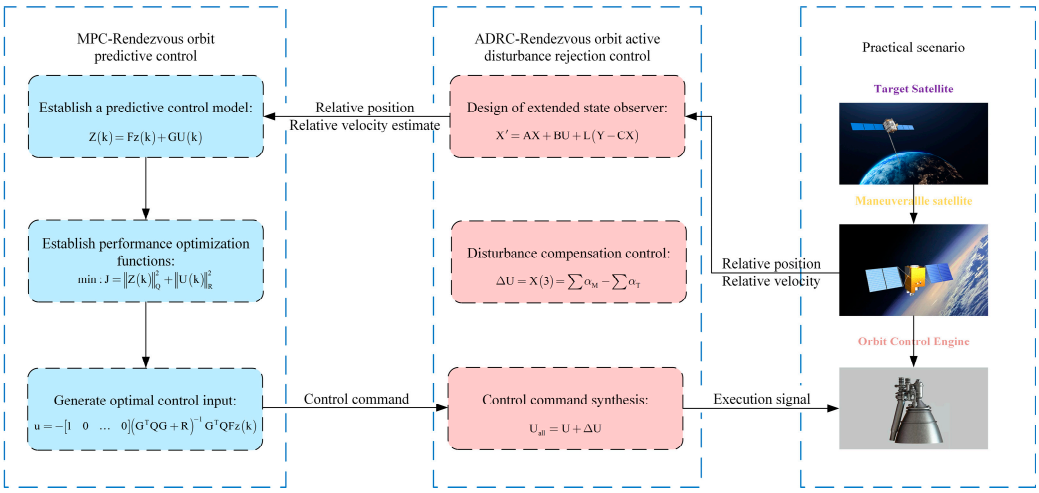


Figure 1. Control structure of ADRC-based predictive control for spacecraft orbital rendezvous.

3.1. Active Disturbance Rejection Control Design

From the relative motion equation of the chaser satellite and the target satellite (Equation (8)), it can be seen that both space perturbation accelerations and unknown maneuvering accelerations of the target satellite introduce deviations in the relative position and relative velocity.

While the magnitude of space perturbation accelerations (e.g., due to J2 effects, atmospheric drag, and solar radiation pressure) is small over typical rendezvous timeframes, their cumulative effects, combined with uncertainties in the target's aerodynamic characteristics and solar radiation reflection coefficients, are difficult to model and predict accurately.

More critically, during rendezvous with a non-cooperative target, the satellite may perform unplanned orbital maneuvers, whose magnitude and direction cannot be directly measured. This unknown maneuvering acceleration is the dominant disturbance in the relative motion dynamics.

The extended state observer (ESO) component of the proposed ADRC-MPC method is designed to estimate the lumped disturbance acceleration, including both space perturbations and unknown target maneuvers. The space perturbation acceleration between the chaser and target satellite as well as the target maneuvering acceleration are collectively defined as the lumped disturbance. The ESO is used to estimate this total disturbance, which is then fed forward as compensation into the control command during the control process, enabling real-time online suppression of the space perturbation acceleration and the target's maneuvering motion. Compared with the traditional active disturbance rejection control (ADRC), the system disturbance in this paper includes both low-frequency, extremely small-magnitude space perturbation acceleration and high-frequency, large-magnitude target maneuvering acceleration. The characteristics of different components in the disturbance vary significantly. For spatial trajectory rendezvous control, it is necessary to accurately and quickly estimate all types of disturbances. In response to this feature, this paper adopts the method of designing the ESO based on pole placement, which can fully solve the problem of precise system control under disturbances with different characteristics.

Considering that the position, velocity, and control variables in the three directions of the geocentric first equatorial coordinate system are mutually independent, state equations are established separately for the X-, Y-, and Z-direction. In these state equations, the state variables are the relative position, relative velocity, and total disturbance; the input is the control acceleration of the chaser satellite; and the output variables are the relative position and relative velocity measured by the radar seeker.

The state observation equation is as follows:

$$\begin{cases} \dot{\boldsymbol{X}}_{\boldsymbol{1}} = \boldsymbol{A}_1\boldsymbol{X}_1 + \boldsymbol{B}_1\boldsymbol{U}_1 \\ \boldsymbol{Y}_1 = \boldsymbol{C}_1\boldsymbol{X}_1 \end{cases}, \begin{cases} \dot{\boldsymbol{X}}_2 = \boldsymbol{A}_2\boldsymbol{X}_2 + \boldsymbol{B}_2\boldsymbol{U}_2 \\ \boldsymbol{Y}_2 = \boldsymbol{C}_2\boldsymbol{X}_2 \end{cases}, \begin{cases} \dot{\boldsymbol{X}}_3 = \boldsymbol{A}_3\boldsymbol{X}_3 + \boldsymbol{B}_3\boldsymbol{U}_3 \\ \boldsymbol{Y}_3 = \boldsymbol{C}_3\boldsymbol{X}_3 \end{cases} \tag{9}$$

Among them:

$$\boldsymbol{X}_1 = \begin{bmatrix} \Delta V_x \\ \Delta x \\ \Delta a_x \end{bmatrix}, \boldsymbol{X}_2 = \begin{bmatrix} \Delta V_y \\ \Delta y \\ \Delta a_y \end{bmatrix}, \boldsymbol{X}_3 = \begin{bmatrix} \Delta V_z \\ \Delta z \\ \Delta a_z \end{bmatrix} \tag{10}$$

$$\boldsymbol{U}_1 = u_{Mx}, \boldsymbol{U}_2 = u_{My}, \boldsymbol{U}_3 = u_{Mz} \tag{11}$$

$$\boldsymbol{Y}_{\boldsymbol{1}} = \begin{bmatrix} \widetilde{\Delta V_x} \\ \widetilde{\Delta x} \end{bmatrix}, \boldsymbol{Y}_2 = \begin{bmatrix} \widetilde{\Delta V_y} \\ \widetilde{\Delta y} \end{bmatrix}, \boldsymbol{Y}_3 = \begin{bmatrix} \widetilde{\Delta V_z} \\ \widetilde{\Delta z} \end{bmatrix} \tag{12}$$

$$\begin{cases} \Delta V_x = Vx_M - Vx_T \\ \Delta x = x_M - x_T \\ \Delta a_x = \sum_{i=1}^{5} A_{Mxi} - \sum_{i=1}^{6} A_{Txi} \end{cases}, \begin{cases} \Delta V_y = Vy_M - Vy_T \\ \Delta y = y_M - y_T \\ \Delta a_y = \sum_{i=1}^{5} A_{Myi} - \sum_{i=1}^{6} A_{Tyi} \end{cases}, \begin{cases} \Delta V_z = Vz_M - Vz_T \\ \Delta z = z_M - z_T \\ \Delta a_z = \sum_{i=1}^{5} A_{Mzi} - \sum_{i=1}^{6} A_{Tzi} \end{cases} \quad (13)$$

In Equation (8), $\Delta\dot{V}_x$, $\Delta\dot{V}_y$, and $\Delta\dot{V}_z$ contain not only the space perturbation acceleration and maneuvering acceleration of the chaser satellite but also the space perturbation acceleration and maneuvering acceleration of the target satellite. The disturbance acceleration is difficult to accurately model and measure, and the timing, form, and overload magnitude of the target's evasive maneuvers are unpredictable. The uncertainty of system model parameters poses technical challenges for orbital rendezvous control with non-cooperative targets.

$\Delta\widetilde{x}$, $\Delta\widetilde{y}$, and $\Delta\widetilde{z}$ are the observed values of the relative positions and velocities in three directions between the chaser satellite and the target satellite in the geocentric first equatorial coordinate system, where $\Delta\widetilde{V}x$, $\Delta\widetilde{V}y$, and $\Delta\widetilde{V}z$ are the observed values of the relative velocities between the chaser satellite and the target satellite. The above parameters are obtained through conversion of the measured parameters from the chaser satellite's seeker, and the conversion relationship is as follows:

$$\begin{bmatrix} \Delta x \\ \Delta y \\ \Delta z \end{bmatrix} = \boldsymbol{C}_b^d \boldsymbol{C}_r^b \begin{bmatrix} \Delta\hat{x}_r \\ \Delta\hat{y}_r \\ \Delta\hat{z}_r \end{bmatrix}, \begin{bmatrix} \Delta V_x \\ \Delta V_y \\ \Delta V_z \end{bmatrix} = \boldsymbol{C}_b^d \boldsymbol{C}_r^b \begin{bmatrix} \Delta\hat{V}x_r \\ \Delta\hat{V}y_r \\ \Delta\hat{V}z_r \end{bmatrix} \quad (14)$$

$\Delta\hat{x}_r$, $\Delta\hat{y}_r$, $\Delta\hat{z}_r$, $\Delta\hat{V}x_r$, $\Delta\hat{V}y_r$, and $\Delta\hat{V}z_r$ are the relative position and relative velocity measured by the chaser satellite's seeker, respectively; $\boldsymbol{C}_r^b$ is the transformation matrix between the seeker measurement coordinate system and the satellite body coordinate system; $\boldsymbol{C}_b^d$ is the transformation matrix between the satellite body coordinate system and the geocentric first equatorial coordinate system.

In the above equation, the nonlinear terms include r_M^3, r_T^3, $\sum_{i=1}^{5} A_{Mxi}$ and $\sum_{i=1}^{5} A_{Txi}$. Two treatments are implemented during model linearization:

① $\sum_{i=1}^{5} A_{Mxi}$ and $\sum_{i=1}^{5} A_{Txi}$ are regarded as lumped disturbances and estimated by the extended state observer (ESO);

② Under the premise that the distance difference between the chaser and the target is much smaller than the distance from the chaser to the geocenter, we assume that $r_M \approx r_T$.

For the above approximation condition, the deviation of control variables induced by linearization is less than 10% when the relative distance between the chaser and the target is no more than approximately 210 km, which validates the applicability of the linearized model.

Selection of linearization equilibrium point: The initial orbital altitude difference between the chaser and target satellite is set to 500 m.

The coefficients of the state equation can be simplified as follows:

$$\boldsymbol{A}_1 = \boldsymbol{A}_2 = \boldsymbol{A}_3 = \begin{bmatrix} 0 & -\frac{\mu}{r_M^3} & 1 \\ 1 & 0 & 0 \\ 0 & 0 & 0 \end{bmatrix}, \boldsymbol{B}_1 = \boldsymbol{B}_2 = \boldsymbol{B}_3 = \begin{bmatrix} 1 \\ 0 \\ 0 \end{bmatrix}, \boldsymbol{C}_1 = \boldsymbol{C}_2 = \boldsymbol{C}_3 = \begin{bmatrix} 1 & 0 & 0 \\ 0 & 1 & 0 \end{bmatrix} \quad (15)$$

Based on the state equation of the system, the following extended state observer (ESO) is constructed:

$$\dot{\hat{\boldsymbol{X}}} = \boldsymbol{A}\hat{\boldsymbol{X}} + \boldsymbol{B}\boldsymbol{U} + \boldsymbol{L}\left(y - \boldsymbol{C}\hat{\boldsymbol{X}}\right) \tag{16}$$

L are design parameters of the extended state observer (ESO), and H is a 3×2 matrix.

Assumption 1. *The initial values of the system disturbance quantity and estimation error are bounded, i.e.,*

$$\begin{aligned} &\sup_{k\geq 0}\|\Delta a_x\| \leq M_x \\ &\sup_{k\geq 0}\|\Delta a_y\| \leq M_y \\ &\sup_{k\geq 0}\|\Delta a_z\| \leq M_z \\ &\|\mathrm{x}(0) - \hat{\mathrm{x}}(0)\| \leq \rho_0 n \end{aligned}$$

Among them, M_x , M_y , M_z and ρ_0 are positive constants.

Lemma 1 ([1]). *Under the conditions of Assumption 1, considering the system Equations (9)–(13) and the ESO observation Equation (16), with the estimation error set as $\boldsymbol{e}_x = \boldsymbol{X} - \hat{\boldsymbol{X}}$, we have*:

$$\dot{\boldsymbol{e}}_x = \dot{\boldsymbol{X}} - \dot{\hat{\boldsymbol{X}}} = (\boldsymbol{A} - \boldsymbol{L}\boldsymbol{C})\boldsymbol{e} \tag{17}$$

The stability and convergence of the above equations need to satisfy the following expressions:

$$\|\boldsymbol{X} - \hat{\boldsymbol{X}} - \boldsymbol{M}\| \leq \frac{\Gamma}{\lambda},\ t > T \tag{18}$$

Among them, $\lambda = |\mathrm{maxRe}\lambda(\boldsymbol{A} - \boldsymbol{L}\boldsymbol{C})|$.

Γ constant related to the system's initial values, disturbances, the upper bounds of their derivatives of all orders, and time represents the error caused by unobservable disturbances. When the disturbance is a slow variable, the estimation deviation is a small number. Therefore, the stability and convergence of the extended state observer (ESO) can be ensured by adjusting the eigenvalues of $(\boldsymbol{A}-\boldsymbol{L}\boldsymbol{C})$.

So far, the design for estimating the spatial perturbation acceleration between the chaser satellite and the target satellite, as well as the maneuvering acceleration of the target satellite, has been completed. According to the variation characteristics of the disturbance acceleration, the observation bandwidth of the observer is designed by adjusting the ESO parameter $\boldsymbol{L}$, so as to achieve fast and accurate estimation of disturbances.

3.2. Design of Rendezvous Orbit Model Predictive Control

The design steps of rendezvous orbit model predictive control mainly include the construction of a predictive model, rolling optimization design, and feedback correction [12,25]. The specific design process is as follows:

(1) Establishment of Predictive Model

After excluding the spatial perturbation acceleration and the maneuvering acceleration of the target satellite, the relative motion equation between the chaser satellite and the target satellite is given in Equation (9).

Among them,

$$\boldsymbol{X}_1 = \begin{bmatrix} \Delta V_x \\ \Delta x \end{bmatrix}, \boldsymbol{X}_2 = \begin{bmatrix} \Delta V_y \\ \Delta y \end{bmatrix}, \boldsymbol{X}_3 = \begin{bmatrix} \Delta V_z \\ \Delta z \end{bmatrix} \tag{19}$$

$$\boldsymbol{U}_1 = u_{Mx}, \boldsymbol{U}_2 = u_{My}, \boldsymbol{U}_3 = u_{Mz} \tag{20}$$

The above continuous-time state equation $\begin{cases} \dot{\boldsymbol{X}}_i = \boldsymbol{A}_i\boldsymbol{X}_i + \boldsymbol{B}_i\boldsymbol{U}_i \\ \boldsymbol{Y}_i = \boldsymbol{C}_i\boldsymbol{X}_i \end{cases}$ is discretized to obtain:

$$\begin{cases} z(k+1)_i = a_i z(k)_i + b_i u(k)_i \\ y(k)_i = C_i z(k)_i \end{cases}, i = 1, 3 \tag{21}$$

Among them, $a_i = e^{A_i T}$ and $b_i = \frac{e^{A_i T} - 1}{A_i}$.

Starting from time step k, the system applies inputs $u(k)$, $u(k+1)$, …, $u(k+M-1)$, over M time steps; thereafter, the input remains constant. To predict the system's state variables $z(k+1)$, $z(k+2)$, …, $z(k+P)$ over the next P time steps, we have:

$$z(k+1) = az(k) + bu(k) \tag{22}$$

$$z(k+2) = a^2 z(k) + abu(k) + bu(k+1) \tag{23}$$

$$\vdots$$

$$z(k+M) = a^M z(k) + a^{M-1} bu(k) + \ldots + bu(k+M-1) \tag{24}$$

$$\vdots$$

$$z(k+P) = a^P z(k) + a^{P-1} bu(k) + \ldots + (a^{P-M} b + \ldots + b) u(k+M-1) \tag{25}$$

It is expressed in vector form as:

$$\boldsymbol{Z}(k) = \boldsymbol{F} z(k) + \boldsymbol{G}\boldsymbol{U}(k) \tag{26}$$

In the above equation,

$$\boldsymbol{Z}(k) = \begin{bmatrix} z(k+1) \\ \ldots \\ z(k+P) \end{bmatrix}_{(nP \times 1)}, \boldsymbol{U}(k) = \begin{bmatrix} u(k) \\ \ldots \\ u(k+M-1) \end{bmatrix}_{(M \times 1)}, \boldsymbol{F} = \begin{bmatrix} a \\ \ldots \\ a^P \end{bmatrix}_{(nP \times n)} \tag{27}$$

$$\boldsymbol{G} = \begin{bmatrix} b & & 0 \\ \ldots & b & \\ a^{M-1} & \ldots & b \\ \ldots & & \ldots \\ a^{P-1} b & \ldots & \sum_{i=0}^{P-M} a^i b \end{bmatrix}_{(nP \times M)} \tag{28}$$

By discretizing the state equation, a recursive equation for the relative motion state transfer between the chaser satellite and the target satellite is established. This forms a numerical recursive relationship that describes the connection between the acceleration input of the chaser satellite and the changes in relative distance and relative velocity between the chaser satellite and the target satellite, thereby completing the construction of the predictive model.

(2) Rolling Optimization Design and Feedback Correction

During the rendezvous process with a non-cooperative target satellite, in addition to meeting the control accuracy requirements for relative position and velocity at the rendezvous point, it is also necessary to comprehensively consider the rendezvous time

and the propellant for orbital control. For this purpose, the performance optimization function for rendezvous orbit control is established as follows:

$$\boldsymbol{J} = \|\boldsymbol{Z}(k)\|_{\mathrm{Q}}^2 + \|\boldsymbol{U}(k)\|_R^2 \tag{29}$$

The complete constrained MPC quadratic program (QP) optimization problem with all explicit constraints, horizons and terminal cost is defined as below:

Given prediction horizon $P \in \boldsymbol{Z}^+$, control horizon $M \in \boldsymbol{Z}^+$, $M \leq P$, positive definite stage weight matrix $\boldsymbol{Q}$ and terminal weight matrix $\boldsymbol{Q}_f$. At each sampling instant k, the rolling optimization reads:

$$\begin{gathered} \min_{u_{k|k},\ldots,u_{k+M-1|k}} \boldsymbol{J} = \sum_{i=0}^{P-1} \|x_{k+i|k}\|_{\mathrm{Q}}^2 + \|x_{k+P|k}\|_{Q_f}^2 \\ st.\ x_{k+i+1|k} = \boldsymbol{F}x_{k+i|k} + \boldsymbol{G}u_{k+i|k}, i = 0, \ldots, P-1, \\ u_{\min} \leq u_{k+i|k} \leq u_{\max}, i = 0, \ldots, M-1, \text{input thrust constraints} \\ x_{low} \leq x_{k+i|k} \leq x_{high}, i = 0, \ldots, P, \text{approach corridor state constraints} \\ x_{k+P|k} = 0, \text{terminal rendezvous equality constraints.} \end{gathered} \tag{30}$$

Only the first control input $u_{k|k}$ is executed at each sampling step, and the optimization window rolls forward for the next instant. The parameters $P = 40$, $M = 1$; $u_{\min}$ and $u_{\max}$ are thruster saturation limits; x_{low} and x_{high} denote the upper and lower bounds of the safety approaching corridor.

The goal of optimal control is to minimize $\boldsymbol{J}$, subject to $\partial \boldsymbol{J}/\partial t = 0$. Combining Equations (27) and (30), we obtain:

$$\boldsymbol{U}(k) = -\left(\boldsymbol{G}^T\boldsymbol{Q}\boldsymbol{G} + \boldsymbol{R}\right)^{-1}\boldsymbol{G}^T\boldsymbol{Q}\boldsymbol{F}z(k) \tag{31}$$

Let

$$\boldsymbol{G}_Q = \left(\boldsymbol{G}^T\boldsymbol{Q}\boldsymbol{G} + \boldsymbol{R}\right)^{-1}\boldsymbol{G}^T\boldsymbol{Q} \tag{32}$$

Then

$$u = -\boldsymbol{G}_Q x \tag{33}$$

Remark 1. *Equation (31) only provides the analytical closed-form feedback gain under the ideal unconstrained condition where all input and state constraints remain inactive. In actual rendezvous missions with thrust saturation and safety corridor limits, the control sequence is solved numerically via the above constrained quadratic program rather than using this fixed linear gain directly, and the real control command will deviate from $-\boldsymbol{K}x$ to satisfy all hard physical constraints.*

The above equation indicates that the optimal solution for rendezvous orbit control $\boldsymbol{U}(k)$ is obtained by multiplying the gain matrix by the state variables. Among them, the gain matrix is not only related to the state coefficients $\boldsymbol{F}$ and control coefficients G of the system's state equation but also associated with the state gain matrix $\boldsymbol{Q}$ and control gain matrix $\boldsymbol{R}$ in the performance function. By adjusting the numerical values of $\boldsymbol{Q}$ and $\boldsymbol{R}$, the control precision, orbital rendezvous time, and propellant consumption for orbital control can be determined.

Through rolling optimization, the optimal control input parameters from the current time step k to time step $k + M$ are determined, and the immediate optimal control parameter $\boldsymbol{U}(k)$ is expressed as:

$$u(k) = \begin{bmatrix} 1 & 0 & \ldots & 0 \end{bmatrix} \boldsymbol{U}(k) \tag{34}$$

$$u(k) = -\begin{bmatrix} 1 & 0 & \dots & 0 \end{bmatrix} \left(\boldsymbol{G}^T \boldsymbol{Q} \boldsymbol{G} + \boldsymbol{R} \right)^{-1} \boldsymbol{G}^T \boldsymbol{Q} \boldsymbol{F} z(k) \tag{35}$$

Let

$$d = \begin{bmatrix} 1 & 0 & \dots & 0 \end{bmatrix} \left(\boldsymbol{G}^T \boldsymbol{Q} \boldsymbol{G} + \boldsymbol{R} \right)^{-1} \boldsymbol{G}^T \boldsymbol{Q} \tag{36}$$

Then:

$$u(k) = d \boldsymbol{F} z(k) \tag{37}$$

The computational burden of the proposed MPC scheme is determined by the number of optimization variables, equal to the product of control horizon M and three-dimensional control acceleration vector. The primary simulation adopts $M = 1$ to minimize variable dimension and reduce QP solving overhead. As tested in Section 4.3, the single-step average computation delay of the full ADRC-MPC algorithm is only 18 ms on a 2.5 GHz general processor, which satisfies the typical 50~100 ms sampling cycle requirement of space-borne GNC computers. A lightweight active-set quadratic programming solver is utilized without heavy matrix inversion operations, making this control framework feasible for low-power on-orbit embedded hardware deployment.

3.3. Closed-Loop Stability Analysis of the ADRC-MPC System

To verify the convergence and robustness of the proposed ADRC-MPC control architecture, the input-to-state stability (ISS) of the closed-loop system is proven in this section.

Assumption 2. *The lumped disturbance d and its time derivative $\dot{d}$ are uniformly bounded, such that:*

$$\|d(t)\| \le \overline{d}, \ \|\dot{d}(t)\| \le \dot{\overline{d}} \tag{38}$$

where $\overline{d}$ and $\dot{\overline{d}}$ are known positive constants.

The continuous-time nominal disturbance-free relative dynamics are written as $\dot{x} = Ax + Bu$. We discretize the system with zero-order hold under a sufficiently small sampling period T_s, which yields the discrete state recursion:

$$x_{k+1} = Fx_k + Gu_k \tag{39}$$

where $F = e^{AT_s}$ and $G = \int_0^{T_s} e^{A\tau} B d\tau$.

For finite-horizon MPC with prediction horizon P, control horizon M, positive definite weight matrices $Q \succ 0$, and $R \succ 0$, the unconstrained rolling optimization problem reads:

$$\min_{u=[u_0,\dots,u_{M-1}]^T} \boldsymbol{J} = \sum_{i=0}^{P-1} \|x_{k+i}\|_Q^2 + \sum_{i=0}^{M-1} \|u_{k+i}\|_R^2 \tag{40}$$

subject to state and input hard constraints (thrust saturation, approach corridor).

The optimal control sequence is an affine function of the current state $x_k : u^* = -\kappa x_k$. Only the first control input u_0 is applied at each time instant, which defines an equivalent static state feedback law:

$$u_0 = -Kx_k \tag{41}$$

where K denotes the first row matrix of κ. This K is the static feedback gain adopted in subsequent Lyapunov and closed-loop matrix analysis, establishing a rigorous mathematical connection between rolling MPC optimization and the time-invariant linear feedback used in stability proof.

Assumptions for Lemma 1:

(A1) $Q \succ 0$ and $R \succ 0$ are symmetric positive definite weight matrices;

(A2) Prediction horizon P and control horizon M are sufficiently large;

(A3) A robust positively invariant set exists for all admissible states and control inputs within prescribed constraints.

Statement: *Under (A1)–(A3), the discrete closed-loop matrix $F - GK$ is Schur stable; for sufficiently small sampling period T_s , the corresponding continuous closed-loop matrix $A - BK$ is Hurwitz (all eigenvalues lie strictly in the open left half complex plane).*

Proof. When P, $M \to \infty$, finite-horizon MPC degenerates to infinite-horizon LQR control. The LQR gain solves the discrete algebraic Riccati equation (DARE):

$$F^T P_{lyap} F - P_{lyap} - F^T P_{lyap} G (R + G^T P_{lyap} G)^{-1} G^T P_{lyap} F + Q = 0 \tag{42}$$

The unique positive definite solution $P_{lyap} \succ 0$ guarantees $F - GK$ Schur stable. For small T_s, the zero-order hold discretization mapping preserves stability, such that the continuous counterpart $A - BK$ is Hurwitz. □

Remark added to correct original ambiguous statement: Standard constrained MPC without robust positively invariant set design cannot inherently guarantee closed-loop stability. The Hurwitz property of $A - BK$ only holds under Assumptions (A1)–(A3) listed above.

Lemma 2 (ESO Error Convergence)**.** *Define the spectral abscissa of matrix L as*

$$\alpha(L) = \max\{\mathrm{Re}(\lambda) | \lambda \in \sigma(L)\} \tag{43}$$

where $\sigma(L)$ denotes the set of all eigenvalues of L and $\mathrm{Re}(\cdot)$ represents the real part of a complex eigenvalue. The spectral abscissa $\alpha(L)$ governs the exponential decay rate of the ESO observation error.

For the extended state observer designed in Equation (16), the observation error dynamics are globally exponentially stable. The estimation error satisfies:

$$\|e(t)\| \leq \mathrm{K} e^{-\lambda t} \|e(0)\| + \gamma \sup_{\gamma \in [0,t]} \|\dot{d}(\tau)\| \tag{44}$$

where $\mathrm{K} > 0$, $\lambda > 0$, and $\gamma > 0$ are constants fully determined by the observer gain matrix L.

Let $\Lambda = A - LC$ denote the ESO error state matrix. The exponential decay rate λ is determined by the spectral abscissa $\alpha(L)$, i.e., the maximum real part of all eigenvalues of Λ, which is explicitly assigned via pole placement when tuning matrix L in Table 2 of Section 4. The coefficients K and γ are derived from the spectral norm of Λ^{-1}:

$$\mathrm{K} = \|\Lambda^{-1}\|, \ \gamma = \frac{\mathrm{K}}{\lambda} \tag{45}$$

In our numerical simulations (Table 2), the observer gain matrix L yields $\lambda = 1.0$ rad/s and $\gamma = 18.2$, which are consistent with the exponential convergence bounds in Lemma 2. Thus, the observer theoretical parameters are fully matched to simulation parameters.

Thus, the ESO estimation error is uniformly ultimately bounded (UUB).

Theorem 1 (Closed-Loop ISS of ADRC-MPC System)**.** *Consider the relative motion dynamics, ESO, and MPC controller designed in previous sections.*

Suppose that:

1. *The MPC cost function satisfies Assumptions (A1)–(A3) in Lemma 1, so $A - BK$ is Hurwitz;*
2. *The prediction horizon P and control horizon M are sufficiently long;*
3. *Disturbance d and its derivative $\dot{d}$ satisfy Assumption 2 (uniform boundedness).*

Then, the closed-loop ADRC-MPC system is input-to-state stable (ISS) with respect to the ESO estimation error e_d , and the tracking error $x - x_{ref}$ is uniformly ultimately bounded (UUB).

Proof (Complete Small-Gain Derivation with Explicit K_∞ Gain Functions). The closed-loop system forms a cascade interconnection of two ISS subsystems:

- Subsystem S_1: ESO error dynamics, input e_x, output e_d, ISS gain mapping $\gamma_1 \in K_\infty$;
- Subsystem S_2: MPC tracking dynamics, input e_d, output e_x, ISS gain mapping $\gamma_2 \in K_\infty$.

Step 1: Derive ISS gain $\gamma_1(.)$ for ESO subsystem S_1.
From Lemma 2, the disturbance estimation error satisfies:

$$\|e_d(t)\| \leq \gamma_1(\sup_{\tau \leq t}\|\dot{d}(\tau)\|),\ \gamma_1(s) = \frac{K}{\lambda}s \tag{46}$$

$\gamma_1(s)$ is a linear class K_∞ function (strictly increasing, $\gamma_1(0) = 0$).
Step 2: Derive ISS gain $\gamma_2(.)$ for MPC tracking subsystem.
The tracking error dynamics with disturbance estimation error input read:

$$\dot{e}_x = (A - BK)e_x + Be_d \tag{47}$$

Since $A - BK$ is Hurwitz, there exists $P \succ 0$ solving the Lyapunov equation:

$$(A - BK)^T P + P(A - BK) = -I \tag{48}$$

Applying standard ISS Lyapunov analysis, the state error bound satisfies:

$$\|e_x(t)\| \leq \gamma_2(\sup_{\tau \leq t}\|e_d(\tau)\|) \tag{49}$$

$$\gamma_2(s) = \frac{2\|PB\|}{\lambda_{\min}(P)}s \tag{50}$$

$\gamma_2(s)$ is also linear class K_∞.
Step 3: Verify small-gain sufficient condition $\gamma_1 \circ \gamma_2 < id$.
The composite gain mapping is calculated as:

$$(\gamma_1 \circ \gamma_2)(s) = \gamma_1(\gamma_2(s)) = \frac{2K\|PB\|}{\lambda \cdot \lambda_{\min}(P)} \triangleq \alpha s \tag{51}$$

By pole-placement tuning of ESO matrix L and MPC weight matrices Q and R, we can always adjust the constant coefficients such that $\alpha < 1$. For all input norm $s > 0$:

$$(\gamma_1 \circ \gamma_2)(s) = \alpha s < s = id(s) \tag{52}$$

The core small-gain condition is mathematically verified.
Step 4: Final stability conclusion
Per the small-gain theorem for interconnected ISS systems, the cascaded $S_1 - S_2$ closed-loop ADRC-MPC system is input-to-state stable. All state tracking errors and disturbance estimation errors are uniformly ultimately bounded under bounded time-varying lumped disturbances.
This completes the full mathematical proof with all intermediate derivations supplemented. □

Corollary 1. *The tracking error of the ADRC-MPC system will converge to a compact small bounded set under unknown time-varying orbital perturbations and target evasive maneuvers, which guarantees the safety and reliability of non-cooperative target autonomous rendezvous.*

4. Numerical Simulation

4.1. Control Parameter Design

To verify the superiority of the proposed rendezvous orbit predictive control method based on active disturbance rejection, a typical scenario of low-Earth orbit (LEO) rendezvous is established. Simulation analyses are conducted on the estimation performance of the extended state observer (ESO) for both space perturbation acceleration and target satellite maneuvering acceleration. Additionally, the model predictive control method for non-cooperative target space rendezvous orbit based on active disturbance rejection is adopted. Comparative simulations are performed on control indicators including system control accuracy, convergence time, and propellant consumption for orbital control, thereby comprehensively evaluating the applicability of the proposed method.

Simulation Scenario Setup

The total mass of the spacecraft is 350 kg, among which the orbit control engine weighs 50 kg, and 32 kg of working fluid is carried for orbital maneuvering. The specific impulse of the thruster is 225 s. The altitude difference between the chaser satellite and the target satellite is 500 m, with a relative distance of 125 m. The chaser satellite tracks the target satellite, and during the tracking process, the target satellite performs evasive maneuvers in three directions. The chaser satellite relies on relative position and velocity information measured by its seeker to implement orbital rendezvous control. The simulation time step is 1 s.

(1) Constraints

- The thrust of the spacecraft orbital control engine is 50 N, and the engine supports continuous startup and shutdown.
- The detection range of the seeker is no more than 50 km, with a detection azimuth of -90° to 90°.
- Safety corridor: no collision shall occur during the rendezvous. Relative static state is achieved at rendezvous time, with relative distance ≤ 0.5 m and relative velocity ≤ 0.5 m/s.
- The safety corridor is designed with a tolerance of ± 2 km.

(2) Parameter Setting of the Extended State Observer

The core design parameter of the ESO is the observation bandwidth. According to the variation characteristics of the estimated parameters (i.e., the relative position, relative velocity, and disturbance acceleration between the chaser satellite and the target satellite) for the ESO in this study, the observation bandwidth is adjusted by modifying the values of the matrix $\boldsymbol{L}_{3\times 2}$ to alter the eigenvalue distribution of the characteristic polynomial $|(\boldsymbol{A}_{3\times 3} - \boldsymbol{L}_{3\times 2}\boldsymbol{C}_{2\times 3})|$.

The parameters of the state extended observers for the X-, Y-, and Z-direction are listed in Table 2.

Table 2. Parameter selection of the extended state observer.

Parameter Name	Unit	Value
Bandwidth	rad/s	1.0
L_{11}	-	1.8
L_{12}	-	−0.0
L_{21}	-	1.0
L_{22}	-	1.2
L_{31}	-	0.8
L_{32}	-	0.0

(3) Initial Motion Parameters of the Chaser Satellite and Target Satellite

The initial motion parameters of the chaser satellite and target satellite are presented in Table 3.

Table 3. Initial motion parameters of the chaser satellite and target satellite.

Parameter	Unit	Chaser Satellite	Target Satellite
Semi-major axis	km	6870.50	6871.00
Eccentricity	-	0	0
Orbital inclination	°	50	50
Right ascension of ascending node	°	0	0
Argument perigee	°	90	90
True anomaly	°	0	0.001

(4) Measurement Error of the Chaser Satellite's Radar Seeker

The measurement error of the chaser satellite's radar seeker is given in Table 4.

Table 4. Measurement error of the chaser satellite's radar seeker.

Parameter	Unit	Value
Mean ranging error	m	0.1
Ranging error variance (3σ)	m	0.2
Mean velocity measurement error	m/s	0.005
Velocity measurement error variance (3σ)	m/s	0.1

The maximum maneuver overload of the chaser satellite is 1 g, and that of the target satellite is 0.1 g.

Figures 2 and 3 respectively show the comparisons between the estimated values and actual values of the disturbance acceleration in the *X*-, *Y*-, and *Z*-direction obtained by the extended state observer under the conditions of without considering the radar seeker measurement error and with considering the radar seeker measurement error.

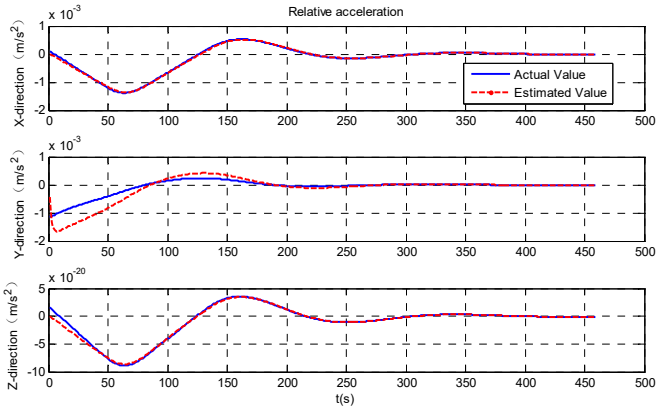


Figure 2. Estimated values of disturbance acceleration in three directions without considering radar seeker measurement error (only orbital perturbations as disturbances).

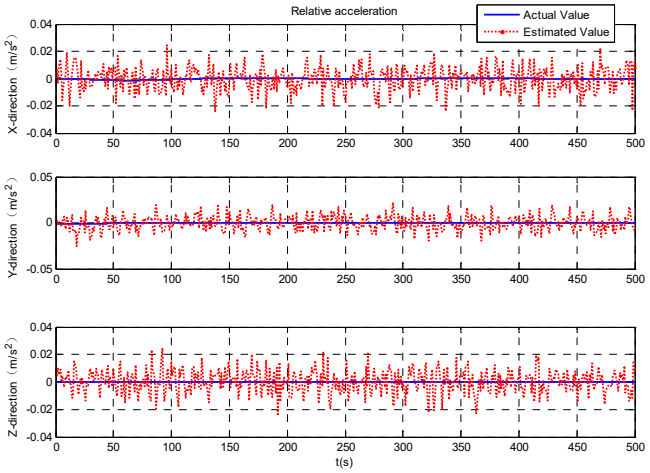


Figure 3. Estimated values of disturbance acceleration in three directions with considering radar seeker measurement error (disturbances: orbital perturbations plus radar measurement errors).

The simulation results in Figures 2 and 3 show that the extended state observer can accurately estimate the variation law of the three-directional disturbance acceleration. When the measurement error of the radar seeker is taken into account, both the relative velocity and position changes in the observed values contain measurement noise, which leads to the introduction of measurement noise into the disturbance acceleration estimation value. However, the median value of the measurement can still be consistent with the actual value.

For the maneuvering problem of non-cooperative targets, sinusoidal, step and ramp disturbances are applied separately to the three axes of the target satellite during tests. Cosine disturbance only has a 90° phase difference from sinusoidal disturbance with identical influence patterns; thus, it is not discussed separately. Restricted by actual physical processes, non-cooperative targets cannot perform pulse-type maneuvers, so pulse disturbance is excluded. Sinusoidal disturbance acceleration is imposed on the X-axis, and its calculation expression is $-0.057 \times \sin(0.1\pi t)$ m/s^2. The disturbance acceleration along the Y-axis is $0.057 - 0.057 \times \sin(0.5\pi t)$ m/s^2. For the Z-axis, ramp disturbance acceleration varies within 0~10 s and remains constant at -0.057 m/s^2 after 10 s. Sinusoidal disturbances at 0.1 Hz (low frequency) and 0.5 Hz (high frequency) are imposed on the X- and Y-axis separately, so as to compare the corresponding influences on the closed-loop control system.

The estimation performance of the extended state observer (ESO) is closely related to its bandwidth and the type of disturbance. A sensitivity analysis of the ESO bandwidth is

carried out for the aforementioned disturbances. Supplementary simulations with distinct ESO bandwidth values (0.1 rad/s, 0.2 rad/s, 0.5 rad/s, and 1 rad/s) have been added to the manuscript. We comprehensively quantify the discrepancies in disturbance estimation performance induced by varying ESO bandwidth under multiple types of disturbances. Figures 4–7 present the actual and estimated disturbance accelerations in the X-, Y-, and Z-directions under different ESO bandwidth configurations, respectively.

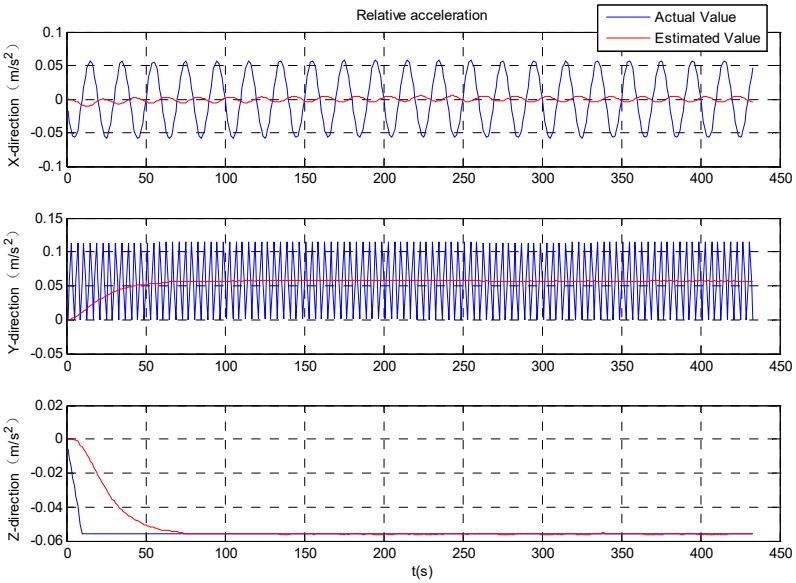


Figure 4. Estimated values of disturbance acceleration (ESO bandwidth values 0.1 rad/s, disturbances: orbital perturbations, radar measurement errors and target maneuvers).

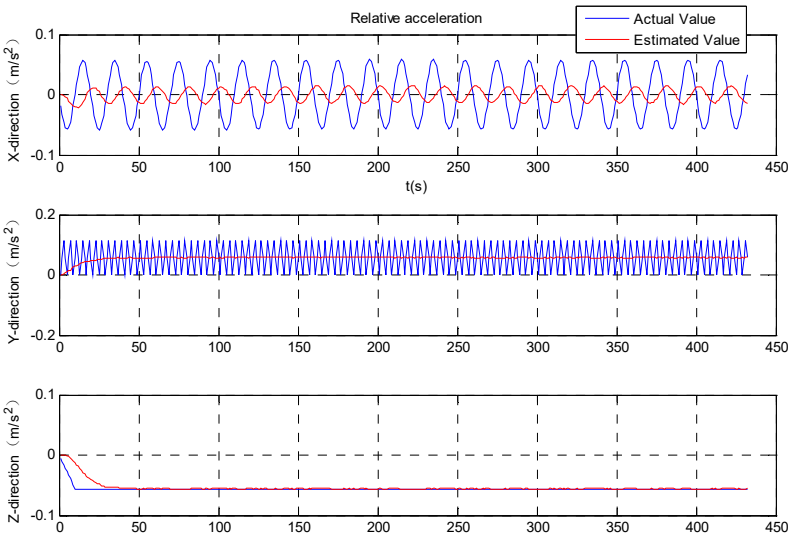


Figure 5. Estimated values of disturbance acceleration (ESO bandwidth values 0.2 rad/s, disturbances: orbital perturbations, radar measurement errors and target maneuvers).

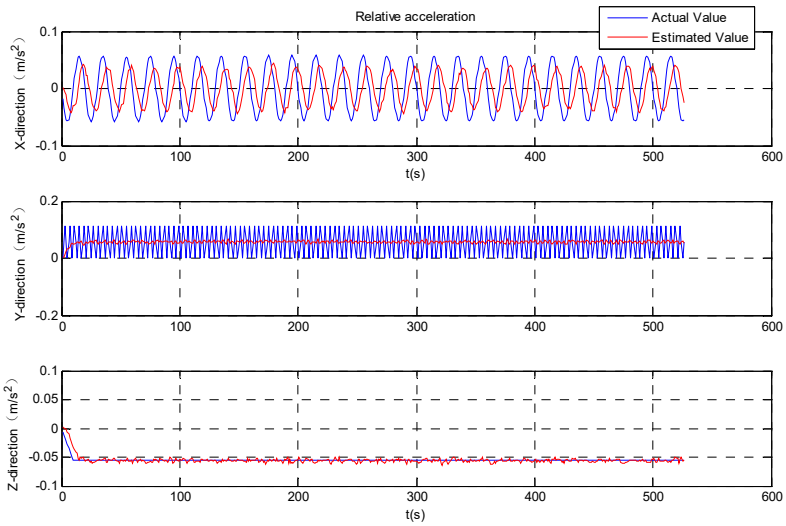


Figure 6. Estimated values of disturbance acceleration (ESO bandwidth values 0.5 rad/s, disturbances: orbital perturbations, radar measurement errors and target maneuvers).

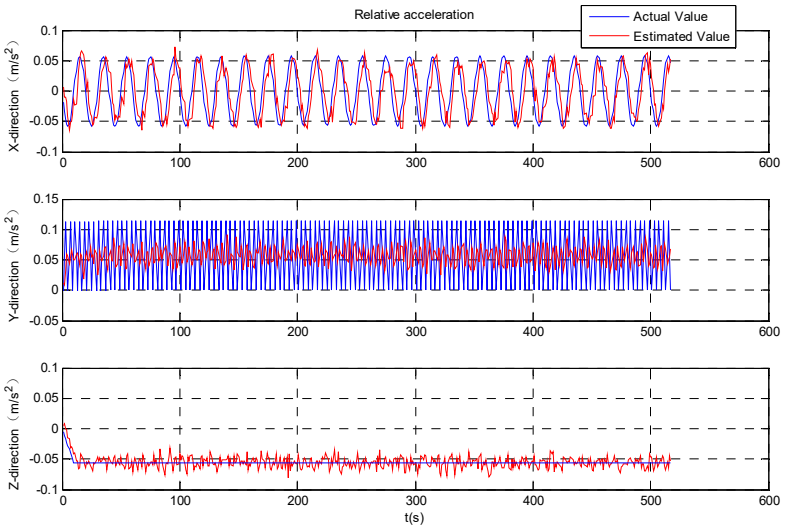


Figure 7. Estimated values of disturbance acceleration (ESO bandwidth values 1 rad/s, disturbances: orbital perturbations, radar measurement errors and target maneuvers).

Comparisons of simulation estimation results under different conditions are summarized in Tables 5 and 6.

Table 5. ESO estimation performance under $0.057 \times \sin(0.1\pi t)$

ESO Bandwidth	0.1 rad/s	0.2 rad/s	0.5 rad/s	1 rad/s
Amplitude attenuation (%)	81	63	38	10
Time delay (s)	9	7	3.6	1.8

Table 6. ESO estimation performance under $0.057 \times \sin(0.5\pi t)$

ESO Bandwidth	0.1 rad/s	0.2 rad/s	0.5 rad/s	1 rad/s
Amplitude attenuation (%)	99	98	92	60
Time delay (s)	9	7	3.6	1.8

The above simulation results reveal that the ESO bandwidth is strongly correlated with the amplitude attenuation and time delay of disturbance estimation. When the ESO

bandwidth is set to 1 rad/s, the amplitude attenuation reaches 10% with a time delay of 1.8 s for medium- and low-frequency disturbance signals. For medium- and high-frequency signals, the amplitude attenuation is 60%, while the time delay remains 1.8 s. Despite the severe amplitude attenuation for high-frequency signals, such signals only induce limited position deviation and exert negligible influence on control performance.

In conclusion, an ESO bandwidth of 1 rad/s is adopted in this paper.

The previous simulation results show that, when the extended state observer is used to estimate the disturbance acceleration, the disturbance estimation value can accurately reflect the variation law of the actual value regardless of whether the disturbance is in the form of spatial perturbation with relatively stable changes or the target maneuvers in different acceleration change forms. Thus, it can be applied to the design of active disturbance rejection control for real-time disturbance compensation.

For the above disturbance forms, the model predictive control method is adopted for rendezvous orbit control. The predictive control parameters are designed according to the characteristics of the controlled object, and the specific values are shown in Table 7.

Table 7. Parameter settings for model predictive control.

Parameter	Value	
	State 1	**State 2**
Control variable step M	1	2
Prediction step P	40	20
State gain matrix Q	I	10I
Control gain matrix R	I	I

Figure 8 presents the relative velocity comparison between the proposed ADRC-MPC method and the baseline standard MPC. Figure 9 shows the corresponding relative position comparison, and Figure 10 illustrates the propellant consumption comparison.

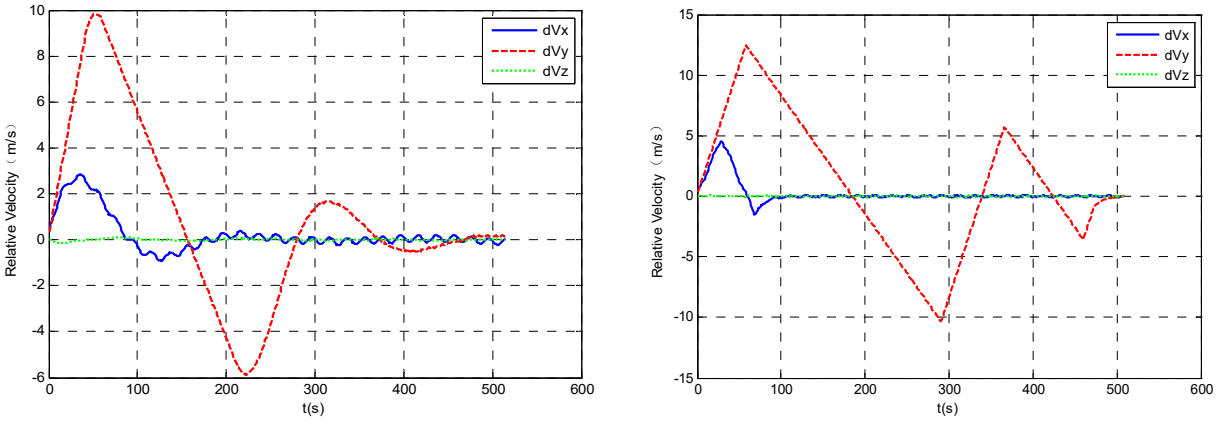


Figure 8. Comparison of relative velocity ((**left**): state 1, (**right**): state 2, disturbances: orbital perturbations, radar measurement errors and target maneuvers).

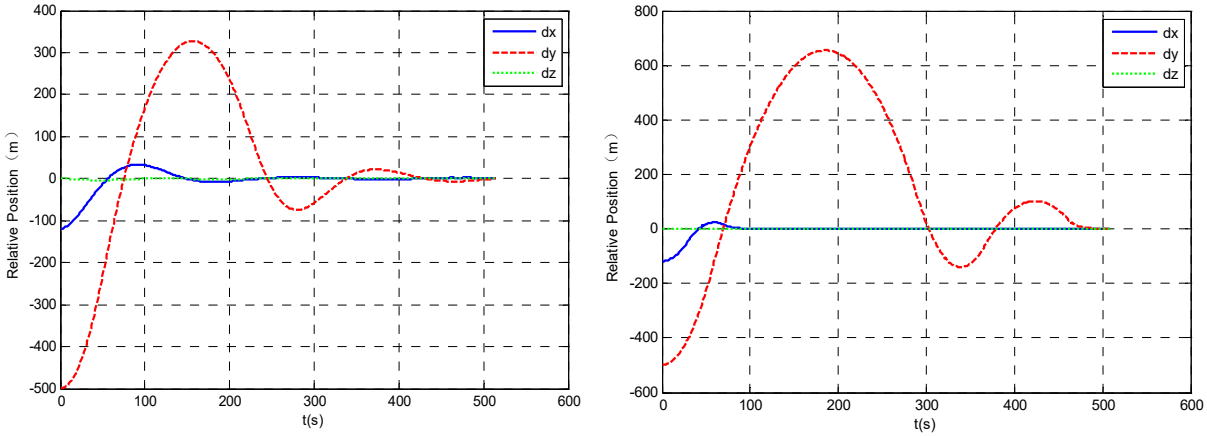


Figure 9. Comparison of relative position ((**left**): state 1, (**right**): state 2, disturbances: orbital perturbations, radar measurement errors and target maneuvers).

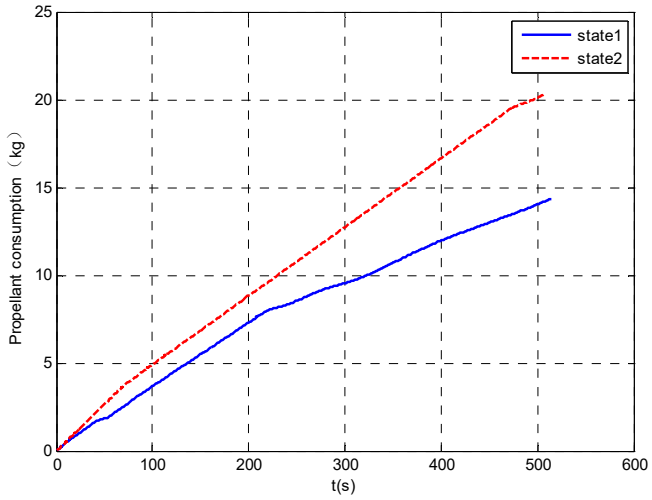


Figure 10. Comparison of orbit control propellant consumption (disturbances: orbital perturbations, radar measurement errors and target maneuvers).

Based on the estimation of spatial perturbation acceleration and target maneuvering acceleration by the extended state observer, after compensation using the active disturbance rejection control method, the influence of disturbance acceleration can be significantly eliminated. Under the two sets of simulation states, the relative position accuracy at the rendezvous point can be controlled within 0.5 m, and the relative velocity error can be controlled within 0.5 m/s, which meets the control accuracy requirements for long-distance rendezvous.

By adjusting the MPC control parameters including matrix M, prediction horizon P, weight matrices Q and R, the tracking performance, control accuracy and propellant consumption can be optimized and tuned. Compared with State 1, State 2 adopts increased values of M and Q as well as a reduced P. Consequently, the controller achieves a more responsive tracking process at the cost of higher propellant consumption. The propellant consumption in State 1 is 14.7 kg, whereas that in State 2 reaches 20.2 kg, The remaining propellant masses are 17.3 kg and 11.8 kg, respectively. Through a comprehensive comparison of the control performance under State 1 and State 2, the MPC parameters adopted in the subsequent simulations are selected according to the configuration of State 1.

4.2. Simulation Comparison of Different Control Methods

To evaluate the performance of the proposed ADRC-MPC method, simulations are carried out for traditional PD control, MPC control and ADRC-MPC control. The parameters of ADRC-MPC are assigned the values of State 2. The control accuracy, settling time and propellant consumption are compared.

Illustrated by the X-direction, the control equation of PD control is as follows:

$$U_x = a_0 \cdot (x_M - x_T) + a_1 \cdot (Vx_M - Vx_T) \tag{53}$$

In the formula, the parameters represent the x-direction position projections of the chaser and target, as well as their x-direction velocity projections respectively. The term refers to the x-direction orbital control command of the chaser, and the other two parameters are PD control gains.

For PD control, the plant under investigation in this paper is a second-order inertial system. The analytical expressions for the system response frequency ω_n and damping ratio ξ are given as:

$$\omega_n = \sqrt{\frac{F}{m}a_0},\ \xi = 2\sqrt{\frac{F}{m}} \cdot \frac{a_1}{\sqrt{a_0}} \tag{54}$$

where F denotes the thrust of the orbit-control engine, m represents the mass of the vehicle, and a_0 and a_1 are the proportional and derivative gains of the PD controller, respectively.

Based on the characteristics of the controlled plant, the system response frequency is set to 0.1 rad/s, and the damping ratio is set to 0.707. Accordingly, the proportional gain a_0 and derivative gain a_1 are calculated to be 0.007 and 0.98, respectively.

Simulation comparisons under this scenario are illustrated in the figure below. Figures 11–13 show the comparison curves of the X-, Y- and Z-directional components of the relative motion velocity between the aircraft and the target under three control methods. Figures 14–16 present the comparison curves of the X-, Y- and Z-directional components of their relative positions. Figure 17 shows the comparison curve of consumed working fluid during orbital rendezvous under three control methods.

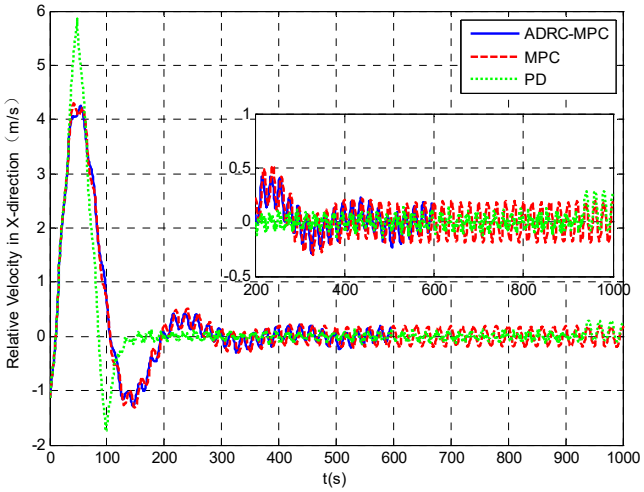


Figure 11. Relative motion velocity between chaser and target in X-direction (disturbances: orbital perturbations, radar measurement errors and target maneuvers).

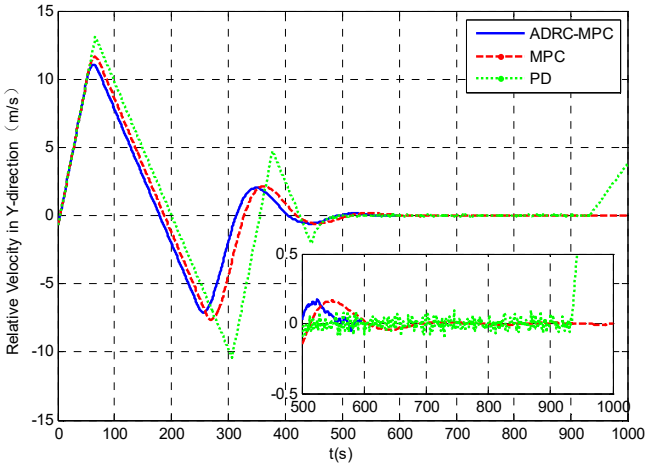


Figure 12. Relative motion velocity between chaser and target in Y-direction (disturbances: orbital perturbations, radar measurement errors and target maneuvers).

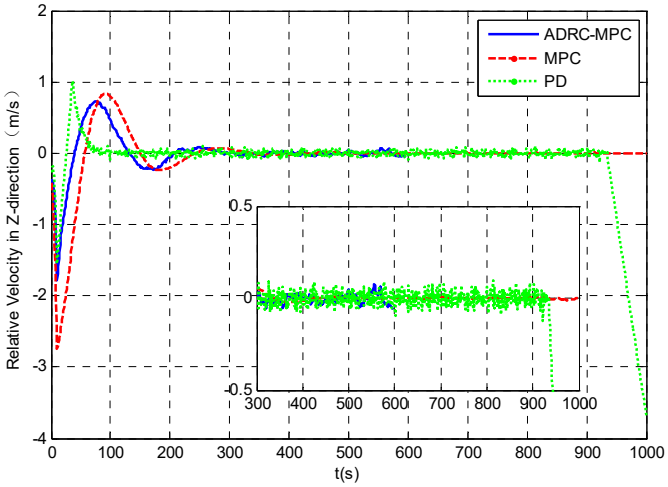


Figure 13. Relative motion velocity between chaser and target in Z-direction (disturbances: orbital perturbations, radar measurement errors and target maneuvers).

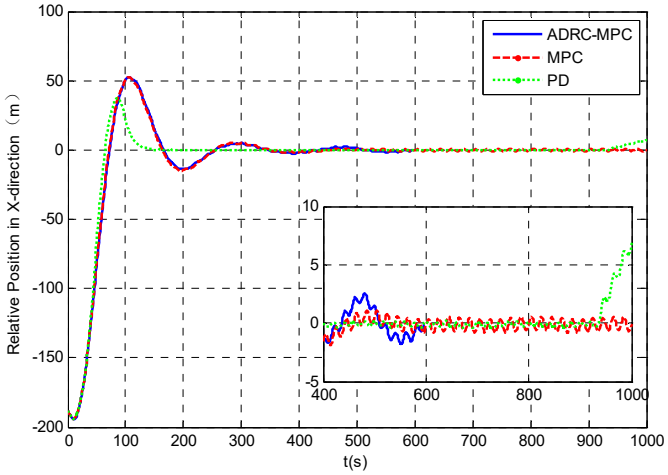


Figure 14. Relative position of chaser and target in X-direction (disturbances: orbital perturbations, radar measurement errors and target maneuvers).

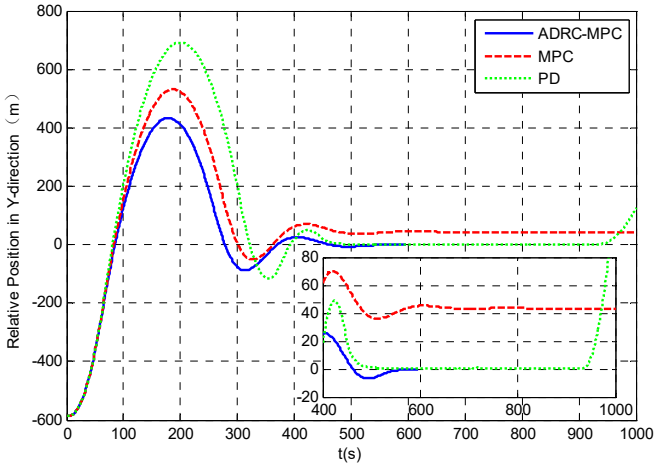


Figure 15. Relative position of chaser and target in Y-direction (disturbances: orbital perturbations, radar measurement errors and target maneuvers).

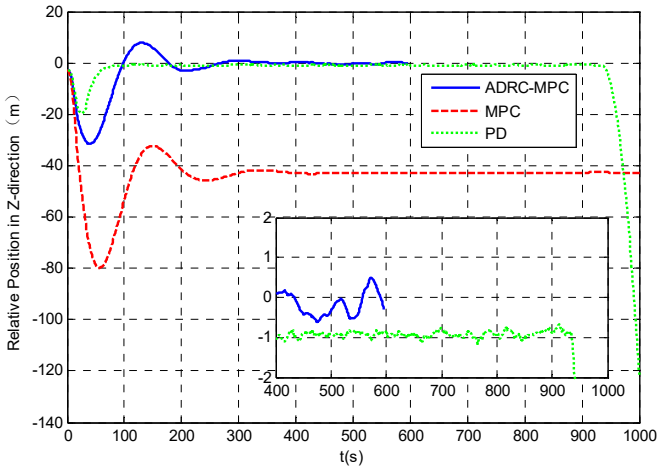


Figure 16. Relative position of chaser and target in Z-direction (disturbances: orbital perturbations, radar measurement errors and target maneuvers).

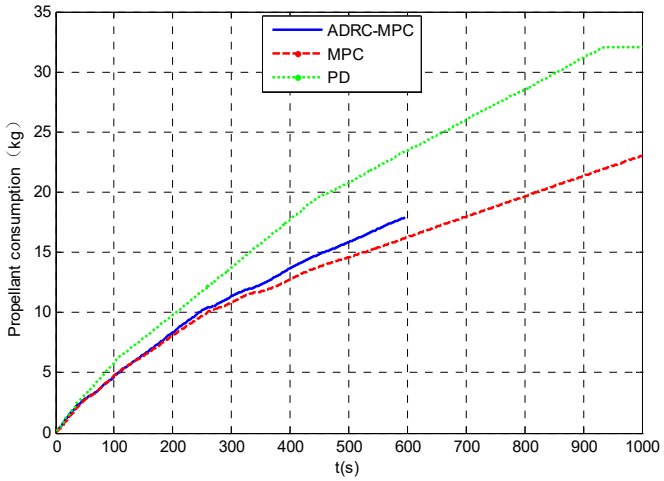


Figure 17. Propellant consumption mass during rendezvous (disturbances: orbital perturbations, radar measurement errors and target maneuvers).

Simulation results of the aforementioned control methods demonstrate that, within the prescribed 1000 s simulation duration, the ADRC-MPC scheme restrains the three-dimensional projections of relative position and velocity between the spacecraft and target

within 0.5 m and 0.5 m/s respectively at 598 s, accomplishing orbital rendezvous with the target. The consumed propellant mass is 17.5 kg, with 14.5 kg of propellant remaining. The control performance of the MPC method is close to that of the MPC-ADRC scheme within the first 500 s. Nevertheless, after eliminating the initial relative position deviation, MPC exhibits poor adaptability to the target disturbance acceleration. The relative position deviations in the Y- and Z-direction remain approximately 40 m and −40 m, respectively, and cannot converge to the range specified by the control requirements. The consumed propellant mass is 23.1 kg, with 8.9 kg of propellant remaining. PD control also cannot fully adapt to the maneuver-induced disturbance acceleration of the target. The relative position in the Z-direction stays at approximately −0.95 m without convergence. Once the propellant consumption of the orbit-control thruster exceeds the available limit of 32 kg, the system loses complete control, and the control error diverges.

The results verify that ADRC-MPC optimizes the tracking transition process and energy consumption. More importantly, ESO can estimate and compensate unknown disturbances without accurate target motion information and precise dynamic models. By contrast, MPC relies heavily on accurate dynamic models of both spacecraft. Though PD control requires no precise target model, it belongs to pure feedback control, leading to persistent tracking lag and incapability of precise rendezvous under continuous target maneuver.

In the simulation, the impact of ESO on the estimation of J2 perturbation and aerodynamic disturbances is not evident due to the short simulation duration. Disturbance effects will become prominent with longer orbital rendezvous time. Orbital variations can reach the kilometer level within a day in low Earth orbit, where the advantages of the ADRC-MPC control method will be more pronounced.

4.3. Monte Carlo Simulation

To verify the robustness of the proposed method, 100 groups of Monte Carlo numerical simulations are carried out under random deviation conditions [32]. The parameter errors considered are as follows: the three-axis initial relative velocity errors between the chaser and non-cooperative target range are within ±2 m/s; the three-axis initial relative position errors are within ±100 m; the thruster deviation of the chaser is ±10%; seeker measurement errors are listed in Table 4. All errors follow uniform distribution in each simulation. Variation curves of three-axis relative velocity and position projections with rendezvous time are obtained from the 100 random simulation cases.

The comparison curves of X-, Y- and Z-directional components of relative motion velocity between the aircraft and target obtained from 100 groups of Monte Carlo simulations are shown in Figures 18–20. The comparison of three-directional components of relative motion position is presented in Figures 21–23. The curves of propellant mass consumption for orbital control versus rendezvous time in 100 simulation cases are shown in Figure 24.

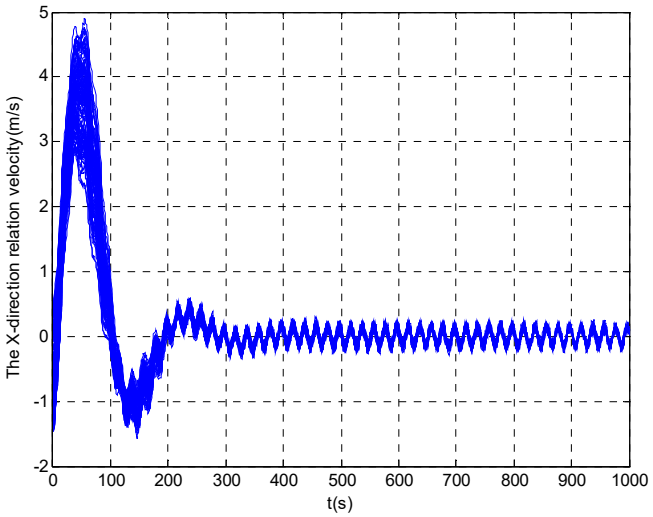


Figure 18. Variation curves of X-direction relative velocity under 100 simulation cases (disturbances: orbital perturbations, radar measurement errors, target maneuvers, initial position and velocity errors).

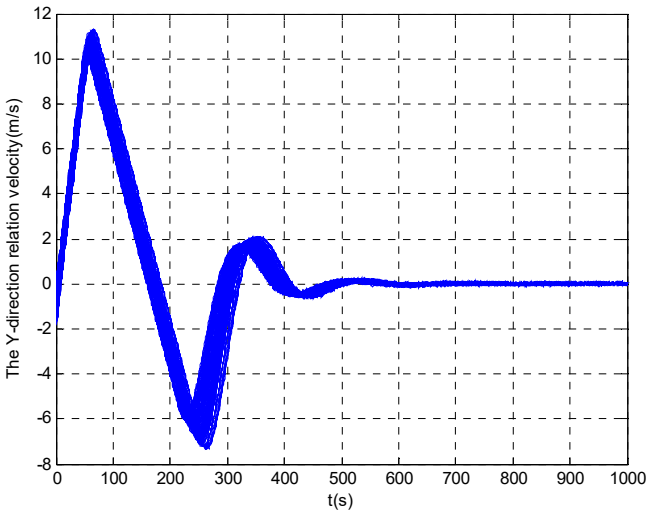


Figure 19. Variation curves of Y-direction relative velocity under 100 simulation cases (disturbances: orbital perturbations, radar measurement errors, target maneuvers, initial position and velocity errors).

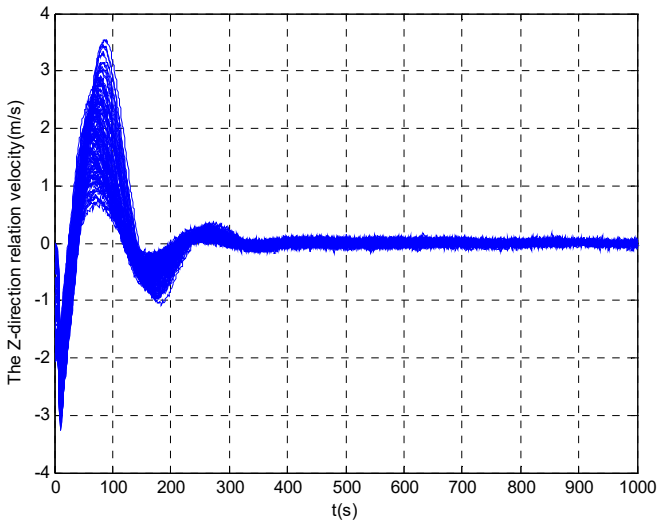


Figure 20. Variation curves of Z-direction relative velocity under 100 simulation cases (disturbances: orbital perturbations, radar measurement errors, target maneuvers, initial position and velocity errors).

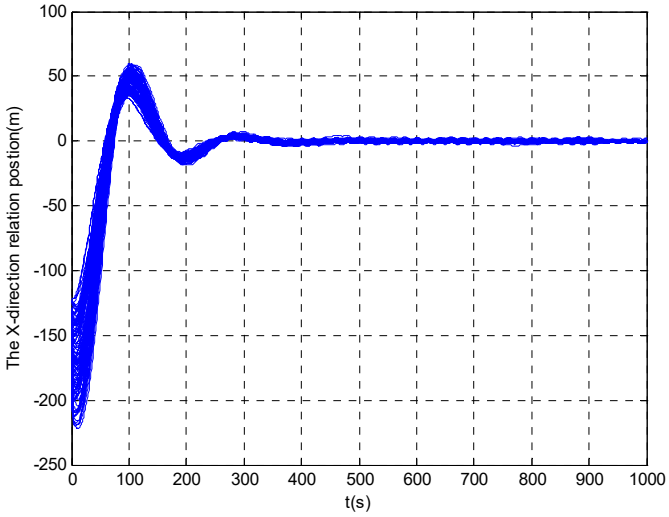


Figure 21. Relative motion position of X-direction under 100 simulation cases (disturbances: orbital perturbations, radar measurement errors, target maneuvers, initial position and velocity errors).

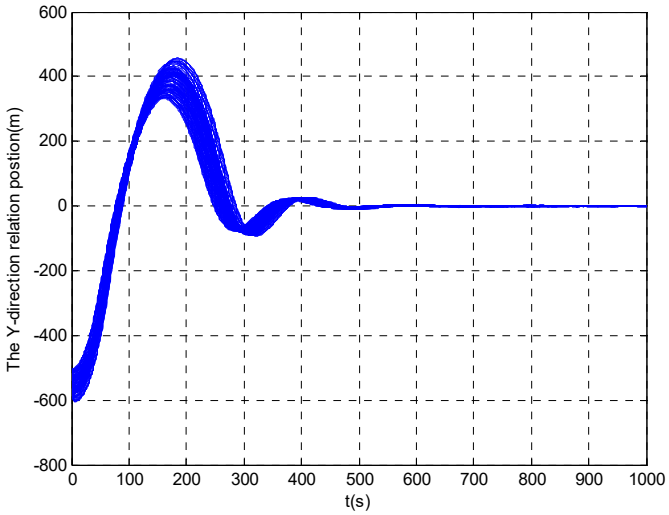


Figure 22. Relative motion position of Y-direction under 100 simulation cases (disturbances: orbital perturbations, radar measurement errors, target maneuvers, initial position and velocity errors).

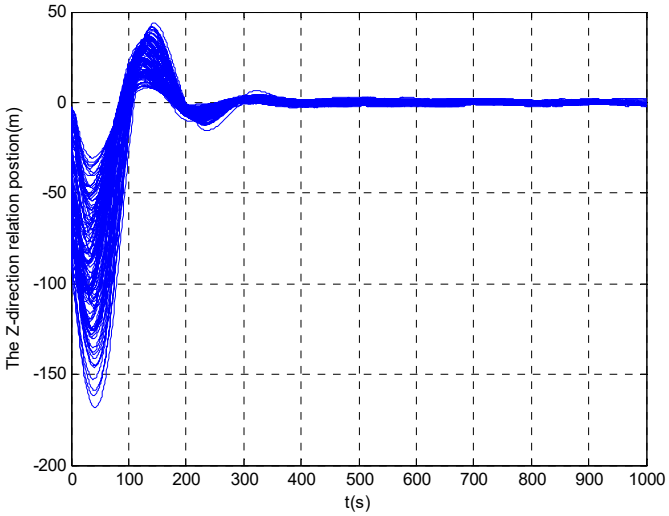


Figure 23. Relative motion position of Z-direction under 100 simulation cases (disturbances: orbital perturbations, radar measurement errors, target maneuvers, initial position and velocity errors).

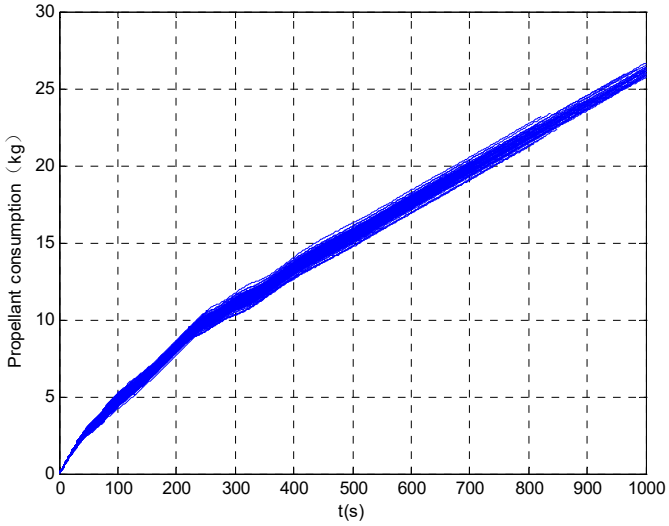


Figure 24. Comparison curve of consumed working fluid from 100 groups of Monte Carlo simulations (disturbances: orbital perturbations, radar measurement errors, target maneuvers, initial position and velocity errors).

The statistical results of 100 groups of random Monte Carlo simulations are shown in Table 8.

Table 8. Statistical results of RMSE and peak error of relative position and velocity in 100 groups of Monte Carlo simulations.

	Unit	RMSE	Peak Error
simulation time	s	771.7	1000.0
X-direction relative velocity	m/s	0.1125	0.2282
Y-direction relative velocity	m/s	0.0889	0.4467
Z-direction relative velocity	m/s	0.0404	0.0960
X-direction relative position	m	0.4447	2.0975
Y-direction relative position	m	0.4696	1.8344
Z-direction relative position	m	0.4851	2.2488
Propellant consumption	kg	21.2193	26.6632

The simulation results indicate that the root-mean-square error of the X-direction position is 0.4447 m, while its peak error reaches 2.0975 m. The Y-direction position yields an RMSE of 0.4696 m and a peak error of 1.8344 m, and the Z-direction position has an RMSE of 0.4851 m together with a peak error of 2.2488 m. Among the 100 Monte Carlo simulation runs, 81 cases satisfy the accuracy requirements, with relative position error within 0.5 m and relative velocity error within 0.5 m/s. The remaining 19 trials present relative position errors larger than 0.5 m in the X-, Y- and Z-direction, where the maximum position error is 2.2488 m.

In the above simulations, the maximum propellant consumption reaches 26.6632 kg. The minimum allowable residual propellant mass is 5.3368 kg, which is within the allowable available propellant limit of 32 kg.

Through comparative simulations covering various disturbance sources (initial position error, initial velocity error, radar range measurement error, radar velocity measurement error), we conclude that the relative position error at rendezvous exceeding the designed threshold is mainly induced by the radar velocity measurement random error of 0.1 m/s. It reveals that sinusoidal interference exerts the most significant impact on tracking error compared with step and ramp interference when the target maneuvers. To mitigate position errors induced by measurement noise, one feasible approach is to reduce the bandwidth of

the extended state observer (ESO). However, this adjustment introduces inherent trade-offs. The system's adaptability to unknown evasive maneuvers of non-cooperative targets will be weakened, orbital-control propellant consumption will increase by 20–40%, and propellant shortage may emerge under extreme conditions, together with reduced steady-state tracking precision. Therefore, the control parameters in this work are comprehensively balanced over rendezvous precision, propellant consumption and convergence time for the given simulation scenarios. For practical engineering applications, the bandwidth of the active disturbance rejection observer should be designed by comprehensively taking the possible maneuver modes and maneuvering capability of the target into account, so as to achieve accurate estimation of target motion.

The single-step computation has a minimum execution time of 18.000 ms, a mean value of 50.988 ms, a standard deviation of 4.707 ms, and a worst-case execution time of 77.2364 ms. The tests were carried out on a typical consumer laptop equipped with an Intel processor running at 2.5 GHz and memory bandwidth of $\geq$50 GB/s. The results show that the single-step delay is only 50.988 ms on this general-purpose platform, which is well within the typical constraints of onboard computers, verifying the real-time performance and on-orbit feasibility [33].

5. Conclusions

Aiming at the orbital rendezvous control problem of space non-cooperative targets under complex space perturbation and unknown target maneuver, this paper proposes an integrated orbit prediction and control method based on active disturbance rejection and model predictive control and completes dynamic modeling, observer design, constrained controller construction, stability proof and numerical simulation verification. The main conclusions are summarized as follows:

(1) By establishing the chaser–target relative motion dynamic model in the geocentric inertial coordinate frame, the complex space environmental perturbations including J2 non-spherical gravity, atmospheric drag, third-body gravity and solar radiation pressure, as well as the unknown evasive maneuver of non-cooperative target, are integrated into a lumped disturbance. The extended state observer can accurately estimate the time-varying disturbance acceleration in real time and realize feedforward compensation in the control loop, which effectively weakens the dependence of the control system on an accurate dynamic model.

(2) The designed ADRC-MPC framework organically combines the disturbance estimation capability of ESO and the multi-constraint optimal rolling optimization advantage of MPC. It can simultaneously satisfy the physical constraints such as thrust amplitude, approach corridor and safety zone and realize the comprehensive optimization of rendezvous convergence time, position and velocity tracking accuracy and orbit control fuel consumption. Compared with traditional PD control and pure MPC method, the proposed method has smaller overshoot, faster convergence speed and lower propellant consumption under unknown maneuver disturbance.

(3) Based on the small-gain theorem, the closed-loop input-to-state stability of the proposed cascade control system is strictly proved, and the tracking error is uniformly ultimately bounded under bounded time-varying disturbances, which provides a solid theoretical basis for engineering application of the method. Monte Carlo simulation verifies that the algorithm has strong robustness to initial position/velocity deviation, thruster parameter perturbation and seeker measurement error and can still maintain high-precision rendezvous within allowable error bounds.

(4) The single-step calculation delay of the algorithm is only 18 ms on an ordinary PC platform, which meets the real-time requirement of on-board computer, and has

good on-orbit application prospect for active debris removal, on-orbit servicing and close-proximity operation to non-cooperative targets.

In addition, the proposed method still has certain limitations: this paper only considers the orbital plane rendezvous under deterministic maneuver form and does not involve the coupling of orbit and attitude of tumbling non-cooperative target. Subsequent research can further combine attitude-orbit coupled dynamic model, introduce intelligent optimization and adaptive parameter tuning strategy, and carry out hardware-in-the-loop simulation to further promote the engineering implementation of the method.

Author Contributions: Conceptualization, L.D. and Y.Z.; methodology, L.D.; software, L.D.; validation, L.D., Z.J. and Z.Y.; formal analysis, Z.Y.; investigation, Y.Z.; resources, H.W.; data curation, L.D.; writing—original draft preparation, L.D.; writing—review and editing, L.D. and Y.Z.; visualization, L.D.; supervision, H.W.; project administration, Z.J.; funding acquisition, H.W. All authors have read and agreed to the published version of the manuscript.

Funding: This work was supported by the National Key Laboratory of Space Target Awareness (STA2025JKW0202), the Chinese Academy of Sciences Youth Innovation Promotion Association (2022126).

Data Availability Statement: The raw data supporting the conclusions of this article will be made available by the authors on request.

Conflicts of Interest: The authors declare no conflict of interest.

References

1. Zhang, Z.X.; Wang, Y.Y.; Bao, W.M. Approaching trajectory planning with field-of-view constraints. *Acta Aeronaut. Astronaut. Sin.* **2025**, *46*, 331702.
2. Zhu, S.; Gavilan, F.; Wang, X. Robust model predictive control for multi-step short range spacecraft rendezvous. *Adv. Space Res.* **2018**, *62*, 1321–1334. [CrossRef]
3. Huang, Y.; Jia, Y.M. Adaptive fixed-time relative position tracking for non-cooperative spacecraft. *J. Frankl. Inst.* **2017**, *354*, 8461–8489. [CrossRef]
4. Mammarella, M.; Capello, E.; Park, H.; Guglieri, G.; Romano, M. Tube-based robust model predictive control for spacecraft proximity operations. *Aerosp. Sci. Technol.* **2018**, *77*, 585–594. [CrossRef]
5. Huang, Y.; Jia, Y.M. Adaptive fixed-time six-DOF tracking control. *IEEE Trans. Control Syst. Technol.* **2019**, *27*, 1796–1804. [CrossRef]
6. Zhang, J.Q.; Ye, D.; Sun, Z.W.; Liu, C. Extended state observer based robust adaptive control on SE(3) for coupled spacecraft tracking maneuver. *Acta Astronaut.* **2018**, *143*, 221–233. [CrossRef]
7. Xu, Z.; Guo, Y.; Li, J. Optimal guidance and collision avoidance for rotating target spacecraft. *Adv. Space Res.* **2019**, *64*, 2389–2401. [CrossRef]
8. Hartley, E.N.; Trodden, P.A.; Richards, A.G.; Maciejowski, J.M. Model predictive control system design and implementation for spacecraft rendezvous. *Control Eng. Pract.* **2012**, *20*, 925–937. [CrossRef]
9. Quartullo, R.; Bianchini, G.; Garulli, A.; Giannitrapani, A.; Leomanni, M. Robust Variable Horizon Model Predictive Control for Rendezvous with Rotating Target. *J. Guid. Control Dyn.* **2026**, *49*, 112–124. [CrossRef]
10. Weiss, A.; Baldwin, M.; Erwin, R.S.; Kolmanovsky, I. Model predictive control for spacecraft rendezvous and docking: Strategies for handling constraints. *IEEE Trans. Control Syst. Technol.* **2015**, *23*, 1321–1335. [CrossRef]
11. Iskender, O.B. Model Predictive Control for Spacecraft Rendezvous and Docking with Uncooperative Targets. Ph.D. Thesis, Nanyang Technological University, Singapore, 2020.
12. Kasaeian, S.A.; Ebrahimi, M.; Assadian, N. Closed-loop powered-coast-powered predictive guidance for spacecraft rendezvous. *Acta Astronaut.* **2020**, *166*, 507–523. [CrossRef]
13. Li, M.; Ma, X.B. Design and implementation of remote autonomous rendezvous method for spacecraft. *J. Astronaut.* **2017**, *38*, 911–918.
14. Bokor, Á.; Biertümpfel, F.; Seiler, P.; Tóth, R. Robust MPC for spacecraft rendezvous under sector-bounded orbital nonlinearities. *IEEE Control Syst. Lett.* **2025**, *9*, 2567–2572. [CrossRef]
15. Oestreich, C.; Linares, R.; Gondhalekar, R. Tube-Based Model Predictive Control with Uncertainty Identification for Autonomous Spacecraft Maneuvers. *J. Guid. Control Dyn.* **2023**, *46*, 1718–1732. [CrossRef]

16. Specht, C.; Bishnoi, A.; Lampariello, R. Autonomous Spacecraft Rendezvous Using Tube-Based Model Predictive Control. *J. Guid. Control Dyn.* **2023**, *46*, 721–733. [CrossRef]
17. Han, J.Q. From PID to active disturbance rejection control. *IEEE Trans. Ind. Electron.* **2009**, *56*, 900–906. [CrossRef]
18. Huang, Y.; Xue, W.C. Active disturbance rejection control: Ideas, applications and theoretical analysis. *J. Syst. Sci. Math. Sci.* **2012**, *32*, 1287–1307.
19. Shang, W.W.; Zhang, B.; Li, K.K.; Cong, S. Autonomous rendezvous of spacecraft on elliptical orbit based on active disturbance rejection control. In Proceedings of the 35th Chinese Control Conference, Chengdu, China, 27–29 July 2016.
20. Li, C.Y.; Wang, W.; Geng, B.K. Neural adaptive sliding mode tracking control of spacecraft relative motion with input saturation. *J. Frankl. Inst.* **2024**, *361*, 109725.
21. Wang, N.N.; Hao, F. Event-triggered sliding mode control with adaptive neural networks. *Neurocomputing* **2021**, *436*, 184–197. [CrossRef]
22. Worthmann, K.; Mehrez, M.W.; Mann, G.K.I.; Gosine, R.G.; Pannek, J. Interaction of open and closed loop control in MPC. *Automatica* **2017**, *82*, 243–250. [CrossRef]
23. Sarapka, A.S.; Martins, M.A.F.; Odloak, D. Stable distributed MPC with zone control and input targets. *Comput. Chem. Eng.* **2021**, *155*, 107507. [CrossRef]
24. Sun, Z.Q.; Dai, L.; Liu, K.; Xia, Y.Q.; Johansson, K.H. Robust MPC for tracking constrained unicycle robots with additive disturbances. *Automatica* **2018**, *90*, 172–180. [CrossRef]
25. Bai, W.; Xue, W.; Huang, Y.; Fang, H. On extended state based Kalman filter design for a class of nonlinear time-varying uncertain systems. *Sci. China Inf. Sci.* **2018**, *61*, 42201. [CrossRef]
26. Breger, L.; How, J.P. Safe trajectories for autonomous rendezvous of spacecraft. *J. Guid. Control Dyn.* **2008**, *31*, 1478–1489. [CrossRef]
27. Rebollo, J.A.; Vazquez, R.; Alvarado, I.; Limon, D. MPC for tracking applied to rendezvous with non-cooperative tumbling targets. In Proceedings of the 63rd IEEE Conference on Decision and Control, Milan, Italy, 16–19 December 2024; pp. 8264–8269.
28. Cao, K.; Li, S.; She, Y. Dynamics and on-orbit assembly strategies for solar array. *Acta Astronaut.* **2021**, *178*, 881–893. [CrossRef]
29. Liu, Y.; Jiang, B.X.; Lu, J.Q. Event-triggered sliding mode control for spacecraft attitude. *IEEE Trans. Syst. Man Cybern. Syst.* **2022**, *52*, 4562–4573.
30. Gavilan, F. Chance-constrained model predictive control for spacecraft rendezvous. *Control Eng. Pract.* **2012**, *20*, 1235–1244. [CrossRef]
31. Gong, B.C.; Li, W.D.; Li, S. Angles-only initial relative orbit determination. *Astrodynamics* **2022**, *6*, 275–289.
32. Volpe, R. GNC architecture for optimal rendezvous to uncooperative tumbling target. *Acta Astronaut.* **2022**, *195*, 312–325. [CrossRef]
33. Flores-Abad, A.; Ma, O.; Pham, K.; Ulrich, S. A review of space robotics technologies for on-orbit servicing. *Prog. Aerosp. Sci.* **2014**, *68*, 1–26. [CrossRef]

Disclaimer/Publisher's Note: The statements, opinions and data contained in all publications are solely those of the individual author(s) and contributor(s) and not of MDPI and/or the editor(s). MDPI and/or the editor(s) disclaim responsibility for any injury to people or property resulting from any ideas, methods, instructions or products referred to in the content.